POLITECNICO DI TORINO

Master's Degree in Biomedical Engineering

Master's Degree Thesis

Development of multi-layered skin phantoms with embedded perfusable microvasculature for Optical Coherence Tomography Angiography

Supervisors

Prof. Kristen M. MEIBURGER

Dr. Mengyang LIU

Dr. Giulia ROTUNNO

Candidate

Bruna COTRUFO

Academic year 2022/2023

Summary

Tissue-simulating phantoms are crucial in the development of optical imaging techniques, such as Optical Coherence Tomography (OCT), in order to test and compare systems performance, validate simulations and evaluate repeatability and reproducibility. One of the most successful OCT functional extensions is OCT Angiography (OCTA), capable of visualizing the blood flow. Thus, the ideal OCTA phantom should mimic the morphology and optical properties of tissue as well as the vasculature shapes and dimensions with the possibility to perfuse it.

In this work, skin mimicking optical phantoms were developed involving both 3D-printing and casting techniques. Firstly, several vessel models were designed tracing the morphology of healthy and pathological microvasculature. Two photons polymerization (2PP) 3D-printing allowed to print hollow vessels with a resolution down to 0.3-8 µm, depending on the exploited magnification objective. Then, polydimethylsiloxane (PDMS) with different concentrations of black and white silicone pigments was used to simulate the multi-layered skin architecture mimicking the optical properties of both dermis and epidermis. Finally, through an infusion pump, the phantom was accurately perfused with diluted whole milk during OCT volume acquisitions so that OCTA volume could be extracted.

Despite the challenge of faithfully reproducing the real microvasculature, capillary-mimicking vessels were printed with inner diameters from 600 µm down to 8 µm and different levels of morphological complexity were obtained, from a simple three-branches model to an entire capillary network. Also, designing branches at different depths, the penetration depth value of 1.5 mm could be assessed for the employed system. The resin vessel wall thickness was set to be 20 µm and its effect on OCT and OCTA was evaluated without showing significant distortion.
The percentages in weight of black and white pigments in PDMS were respectively set to be 0.18% and 0.36% for dermis and 0.20% and 0.72% for epidermis, even if further tests are needed to optimize the epidermis recipe.
In order to properly process the acquired signals and validate the OCTA results, the relationship between OCTA signal intensity and both flow velocity and interscan time was thoroughly investigated obtaining that, for each interscan time, the OCTA signal averagely reaches a common saturation level, around the value of 0.3 for the intensity-based logarithmic OCTA. Moreover, the interscan time influences the flow velocity from which the saturation level is observed as well as the ability to discriminate velocities.

Considering the results from a velocities range between 0.1 and 80 mm/s, the interscan time of about 4.6 ms that characterizes the employed system resulted to be too long to distinguish slow and fast velocities. Also, intensity-based OCTA algorithms turned out to be more suitable for OCTA extraction on the developed phantoms.
The OCTA volumes were then segmented and compared with the printed models in terms of overlapping percentage, showing the potential of this phantom fabrication approach to test OCT systems as well as OCTA algorithms. Dice similarity coefficients of 64% and 70% were obtained for an healthy and a pathological vasculature mimicking phantom, respectively, mainly due to the projection artifact and the penetration depth.

Further developments include the evaluation of these phantoms to be potentially used as multimodal imaging phantoms considering more imaging techniques, such as photoacoustic imaging (PAI).

Acknowledgements

I would like to express my gratitude to a large number of people for the support throughout this thesis.

To my supervisors Prof. Kristen Meiburger, Dr. Mengyang Liu and Dr. Giulia Rotunno, for the opportunity to work on such an interesting project and their guidance and encouragement throughout it.

To all the people I met at The Center for Medical Physics and Biomedical Engineering at the Medical University of Vienna. In particular, to Lisa Krainz and Giulia Rotunno for the precious hints and the time spent to support me during acquisitions; to Christian Grasl, for the patience and the extreme kindness even after thousands of printings; to the OC-PAI group, for the support throughout the project.

To the guys from office 19/18, for putting up with me and sharing carefree moments; to the 3rd floor "Fools", for all the card games and ping-pong matches; to my university colleagues and lifetime friends.

To all my family, from the youngest to the eldest Bruna.

Contents

List of Figures

Part I

Introduction

1. Optical Coherence Tomography

Optical coherence tomography (OCT) is a non-invasive imaging technique widely used in ophthalmology and dermatology. It exploits light interference to reconstruct the sample reflectivity profile in depth similarly to ultrasound imaging but, instead of using sound waves, it uses light waves to create high-resolution images of the tissues.

Coherence and interference are the fundamental principles of OCT. Two light waves are coherent when they have a fixed phase relationship with each other and the same waveform so that the interference pattern is well-defined. The interval in which this assumption is verified is called *coherence length*. If a light source is characterize by a relatively short coherence length, then it's referred to as *low-coherence* light source. In the next sections will be explained why this feature is crucial for images reconstruction.

A general OCT system is then composed by a low-coherence light source, an interferometry that splits the light into a reference arm and a sample arm and a detector that measures the interference signal between waves reflected from these two arms.

1.1 Low-Coherence Interferometry

Interferometry is an optical measurement technique capable of measuring differences in optical path lengths between a backscattered light from a sample and a backscattered light from a known reference path, both originally splitted from the same source. If the implemented light source is a low-coherence source, then it is referred to as low-coherence interferometry that, as will be described later, can measure absolute distances in contrast to classical interferometry.

One of the most common and simple interferometer configuration is the Michelson interferometer. As shown in Fig. 1.1, a source beam hits a beam splitter. It divides the light source into two different beams: a reference beam directed to a reference mirror and a sample beam directed to the sample. The reflected light beams coming back from both arms are then combined again by the beam splitter and then detected, generally by a photodetector. The interferometer output carries the information about the difference between the reference arm and sample arm path lengths. The way to extract it, i.e. the kind of detector implemented as well as the features of the low-coherence light source and reference mirror, depends on the implemented OCT technique and will be

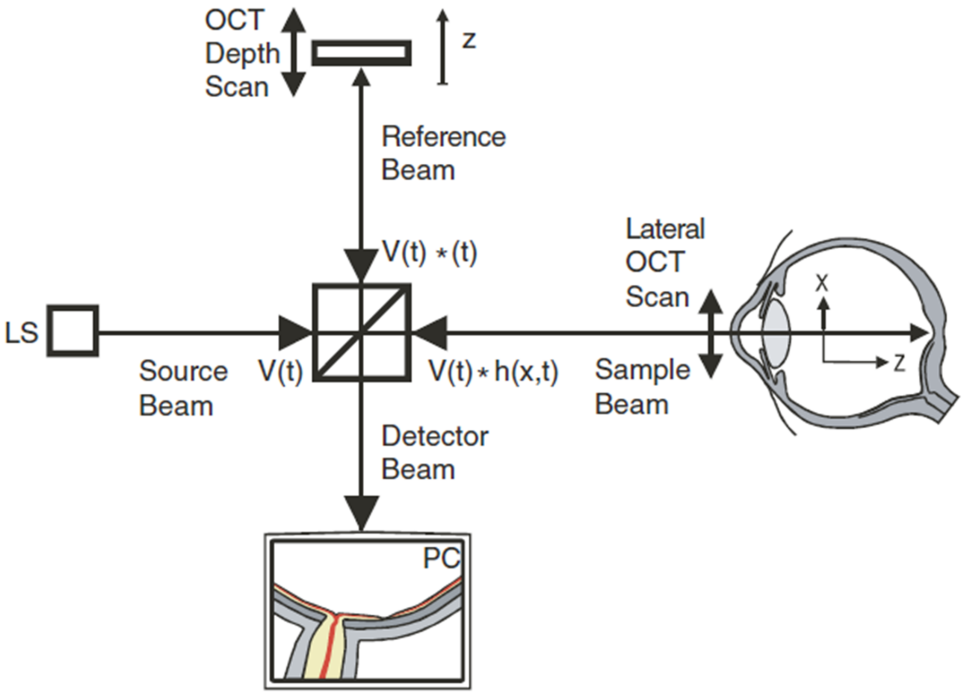

Figure 1.1: Standard OCT scheme based on a low time-coherence Michelson interferometer. Adapted from [1].

discussed later.
In general, the average intensity at the interferometer output is [1]:

$$\langle I_E(t;\Delta t)\rangle = \langle I_S(t)\rangle + \langle I_R(t)\rangle + G_{SR}(\Delta t) \tag{1.1}$$

wherw Δt is the time delay between the beams and G_{SR} the interferogram.

In order to understand why a low-coherence light source is so crucial to locate a scattering object in the sample, let's consider the perfect coherent source: a monochromatic light with a frequency equal to ν_o. The detector beam is the sum of the reference and sample beams, i.e. the interference signal. If the paths lengths from the beam splitter towards the reference mirror and towards the scatterer object in the sample are equal, since the beams are in phase, the interference will be constructive. If the reference mirror is moved by a length d so that at the photodetector the interfering waves are time shifted by half the period in time, then the interference is destructive. However, whenever the time shift became equal to the period in time, or a multiple of it, the interference will be constructive again. It means that with a coherence light source it's impossible to locate the scatterer object. Let's now consider a source with two slightly different frequencies whose difference is equal to $\Delta\nu$. The interference signal is still constructive if the paths lengths are equal but moving the reference mirror the interference signal will be characterized by a beat envelope. Finally, if we consider a broadband source, for example a Gaussian source, the interference signal envelope will

be a single burst and now it's possible to locate the scatterer object simply scanning the reference mirror to investigate each depth. If a scatterer is located at a depth corresponding to the current reference mirror position, then a signal of a certain intensity will be detected. This is the working principle of the so called **Time domain OCT** (TD-OCT), the technology implemented by the early OCT systems.

Thus, a low coherence interferometer allows to extract the position of scatterers inside the sample thanks to phenomenon of interference that occurs only if the path length towards the scatterer is equal to the one towards the reference mirror. Actually, the interference occurs whenever the paths lengths coincide within the so-called **coherence length** l_c, that is indeed the length within which the coherence occurs. It means that l_c is also a measure of the axial resolution related to the localization of the scatterer. l_c is related to the light source spectrum as follow [1]:

$$l_c = \frac{2ln2}{\pi}\frac{\bar{\lambda}^2}{\Delta\lambda} \tag{1.2}$$

where $\bar{\lambda}$ is the mean wavelength and $\Delta\lambda$ the spectral width of the source spectrum under the assumption of a Gaussian spectrum. Considering the previous example, in the case of a monochromatic source $\Delta\lambda \to 0$ causes l_c to be very high so that interferences due to scatterers located at different depths cannot be distinguished, thus it's impossible to localize the depths of the objects. With a broadband source, l_c values of 1-20 μm are typically obtained and the scatter can be localized with an high resolution. Also, the mean wavelength affects the l_c as well and lower $\bar{\lambda}$ leads to better axial resolution. Anyway, it must be taken into account that $\bar{\lambda}$ affects other parameters as well, such as the lateral resolution and the penetration depth.

As described before, with this technique is possible to reconstruct the information in depth, i.e. a mono-dimensional information called A-scan or A-line. In order to obtain a 2D image or a whole volume, a raster scanning is applied (Fig. 1.2). Then, the laser is typically moved along the "fast scanning direction" (x in Fig. 1.2) so that a B-scan image is extracted and then along a "slow scanning direction" (y in Fig. 1.2) obtaining different B-scans at different locations so that the tomography is completely extracted. A 2D image taken along the slow scanning direction is called cross-section. Then, taking all the pixels located within a range of depths, the 2D en-face image is obtained performing for example the mean or the maximum in depth.

1.2 OCT techniques

OCT techniques can be classified in two classes: Time-Domain (TD-OCT) and Fourier Domain (FD-OCT), that can be further classified into Spectral domain OCT (SD-OCT) and Swept-source OCT (SS-OCT).

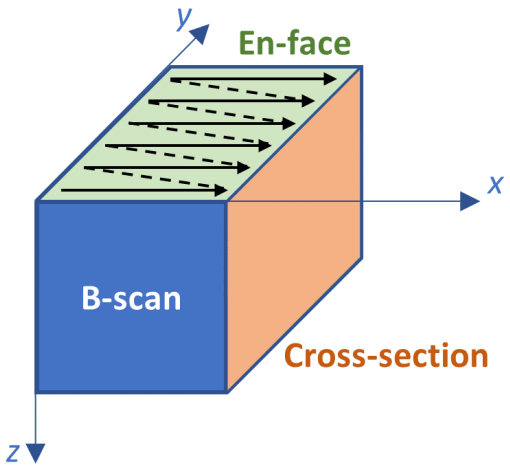

Figure 1.2: OCT volume with B-scan, cross-section and en-face images. The black arrows describe the raster scanning of the whole volume.

1.2.1 Time-domain OCT

As previously stated, in a TD-OCT system the reconstruction of the reflectivity profile in depth is obtained by mechanically scanning the reference mirror in order to investigate a range of depth inside the sample and the resolution of localization at each depth is equal to the coherence length.
Thus, the TD-OCT requires a broadband light source, a moving reference mirror and a single detector. A schematic of a general TD-OCT modality is shown in Fig. 1.3 A. In this modaality, the imaging depth is given by the reference arm travel range.

Even if this technique was widely applied in the early OCT technologies, its main disadvantages is that, since the volume is extracted changing both the laser transversal position respect to the sample and the reference mirror position, the acquisition is extremely time-consuming and also the mechanical movements of components can be an additional noise source.

1.2.2 Fourier-domain OCT

Because of the limitations of time-domain OCT systems, OCT technologies development led to Fourier Domain OCT techniques, mainly the spectral-domain OCT (SD-OCT) and swept source OCT (SS-OCT). In these kind of techniques, the inverse Fourier Transform of the back-scattered light spectrum is used to provide depth-scan information without moving the reference mirror.

Spectral-domain OCT

SD-OCT exploits a broadband light source, a low-coherence interferometer, a spectrometer and an high-speed line scan camera to measure the interference spectrum. A

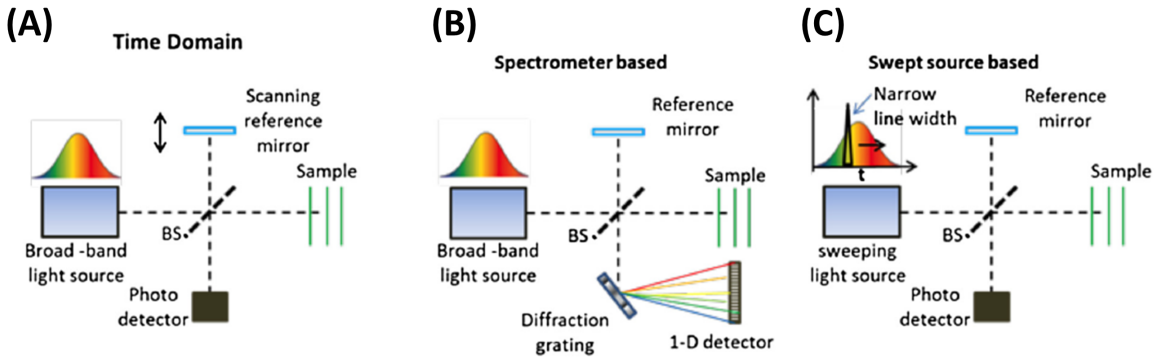

Figure 1.3: Schematic of different OCT modalities. Time domain OCT (A), spectral domain OCT (B) and swept source OCT (C). Adapted from [2].

schematic of a general SD-OCT system is shown in Fig. 1.3 B.

The spectrometer splits the interference signal into different optical frequencies thanks to a diffraction grating. Then, applying the Fourier transform to the detected intensity spectrum is possible to reconstruct the A-scan, i.e. the reflectivity profile of the sample in depth [2]. In particular, shallow reflectors will results in slower variations of the the interference signal over the optical frequencies and vice versa for deeper scatterers. Thus, the weight of each frequency make possible to extract the A-scan without scanning the reference mirror. Then, the imaging depth depends now on the center wavelength λ_o and the spectral resolution (full bandwidth over the number of spectral data points).
This technique allows to obtain better performance respect to TD-OCT in terms of imaging speed, sensitivity and resolution. However, such systems are generally more complex and expensive and are characterized by the sensitivity roll-off, i.e. the gradual loss of sensitivity as a function of depth.

Swept-source OCT

SS-OCT uses a sweeping laser source and a single photo detector instead of a broadband light source and a spectrometer. The swept laser produces a narrowband light source that sweeps through a range of frequencies, allowing for high-speed and high-resolution imaging. A general SS-OCT system is shown in Fig. 1.3 C.
The main advantages of this approach are the higher imaging speed, the possibility to have a more compact fiber-based setup, better performances in terms of SNR and the roll-off effect is reduced. Also, SS-OCT typically works with longer wavelength, resulting in less scattering and better penetration depth.

1.3 OCT system features

Axial and lateral resolution

The axial resolution depends on the coherence length that was previously discussed. Typically, resolution of 5-15 μm can be achieved, depending on the OCT modality and the laser source.
The lateral resolution depends on the the sample arm design and it can be calculated with the Abbe's criteria using the numerical aperture (NA) of the objective lens [2]:

$$\Delta x = \frac{2\lambda_o}{NA} \tag{1.3}$$

Values of 10-30 μm are typically achieved.

Depth of focus

The depth of focus is twice the Rayleigh range and can be calculated as follow [2]:

$$2z_R = \frac{0.61\lambda_o n}{NA^2} \tag{1.4}$$

with n the refractive index. Then, increasing the NA increases the resolution but the depth of focus decreases quadratically. A compromise between the lateral resolution and the depth of focus has to be found.

Penetration depth

OCT penetration depth is significantly affected by light scattering within biological tissue that, in turn, depends on the wavelength. The presence of hemoglobin and melanin in biological tissues usually leads to absorption in the visible and near-IR wavelength range and also, between 800 nm and 1800 nm, scattering and water absorption are the predominant mechanisms. Since scattering decreases for longer wavelengths, better image penetration depth can be achieved with wavelength above 1300 nm, obtaining imaging depths of 1 - 2 mm [2].

2. Optical Coherence Tomography Angiography

OCT signal alone provides morphological information about the target volume based only on back-scattering, without tissue specificity. In order to extract dynamic information as well, the most successful OCT extension is the optical coherence tomography angiography (OCTA), capable of visualizing blood flow or rather the microvascular network. In dermatological applications, thanks to the possibility to extract in a non-invasive manner the tissue and vascular morphologies and the information about blood flow, skin disease diagnoses can benefit from OCTA. Furthermore, in order to objectively describe the complexity of the vascular network, quantitative parameters can be automatically extracted as well [3].
The general idea is to acquire multiple scans at the same location. Comparing consecutive A-scan it's possible to highlight the blood flow respect to the static tissue. The protocol to acquire multiple scans and the ways to compare them will be discussed below.

2.1 OCTA scanning protocols

The multiple acquisition of the same A-line can be performed either acquiring multiple OCT A-scans at the same position before switching to the next lateral position (MB-scan, Fig. 2.1a) or multiple OCT B-scans at the same position before switching to the next location (BM-scan or interframe scan, Fig. 2.1b) or scanning the whole volume before repeating the acquisition [4]. By comparing OCT frames acquired at the same location but in different moments, the signal from stationary tissues should not change, except for random noise. Scatterers moving from voxel to voxel in the target volume, on the contrary, lead to variations in OCT signal. Considering the superficial skin layers, the only moving object should be the flowing blood into capillaries and in particular the red blood cells it contains. Ideally, the comparison of more volumes makes the signal extraction easier but obviously it requires a longer acquisition time, then the motion artifact will be more likely. Typically, comparing four or five volumes is a good compromise between the quality of the extracted OCTA signal and the acquisition time. The employed protocol affects the acquisition time as well but at the same time different protocols imply a different interscan time, i.e. the elapsed time between two consecutive acquisitions at the same location. As will be described later, the interscan

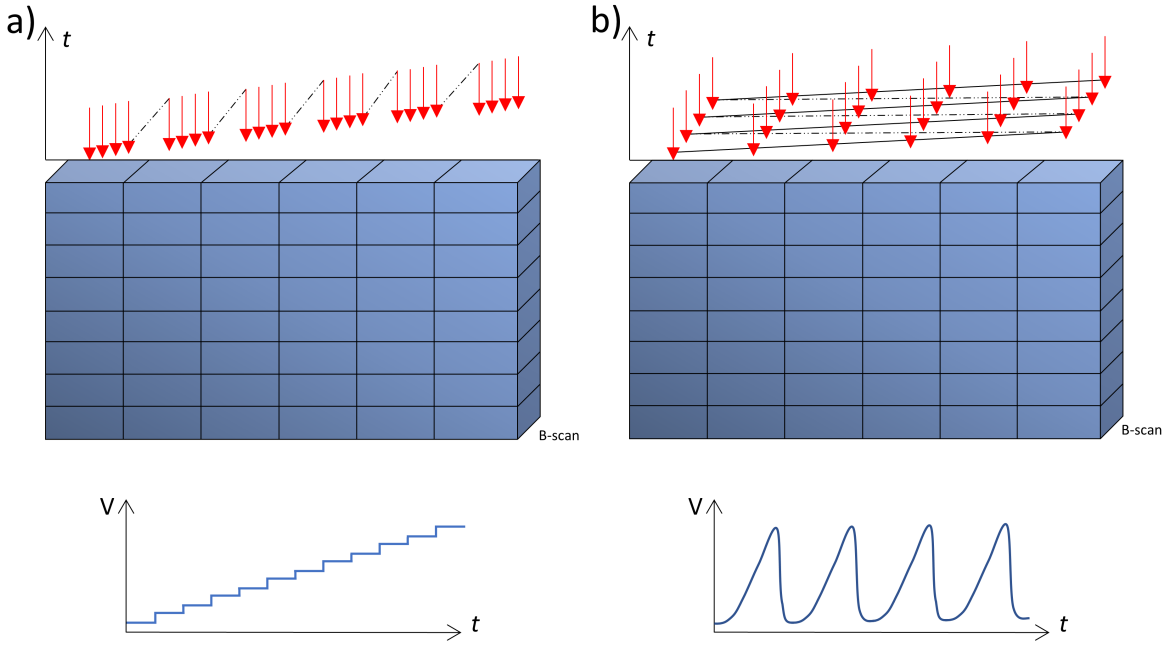

Figure 2.1: OCTA acquisition protocols. Red arrows symbolize A-lines acquisition over time with a MB-scan protocol (a) and a BM-scan or interframe scan protcol (b). In both these examples, four repetitions of the same B-scan are acquired. In the lower part of both sections is showed the approximately shape of the voltage signal sent to the galvo mirrors to obtain that protocol.

time directly affects the OCTA signal and it must be taken into account depending on the application.

2.2 Algorithms

In order to understand in which way is possible to compare consecutive scans, the phenomena of moving backscattering objects must be analyzed.

The flowing blood that generates an OCTA signal is composed of several kinds of cells and particles. However, red blood cells (RBCs) have a refractive index dissimilar to the plasma and the typical hematocrit value is large, about 45%. Thus, RBCs represent the principal scatterers in blood [4]. As will be described in chapter 4.3, a simple FFT yields the A-lines of the complex OCT signal as a function of depth. The complex OCT signal carries the information of the back-scattered light from both static and dynamic scatterers. The contribution from dynamic scatterers changes depending on the movement of the scatterer itself. If the velocity vector characterizing the movement has a component parallel to the sample beam, then the effect on the complex OCT signal is the "Doppler phase shift", i.e. a linear phase shift over time. Otherwise, when the movement has a transverse component or it's a rotation, it implies "decorrelation", i.e. a random change of the complex OCT signal both in intensity and phase. In a

vasculature both these effects are present in different shades [4]. Checking for changes in signal intensity or phase, dynamic scatterers can highlight the vasculature.

2.2.1 Intensity-Based OCTA

The intensity-based OCTA (iOCTA) exploits the magnitude of the complex OCT signal obtained from the Fourier transform of the detected spectral data. Intensity-based approaches allow for more robust and easier implementations because of their lower sensitivity to phase noise and trigger jitter. A general intensity-based technique can be written as:

$$I_{iOCTA}(x, y, z) = \frac{1}{N-1} \sum_{i=1}^{N-1} |A(x, z)_{i+1} - A(x, z)_i| \tag{2.1}$$

where A is the amplitude of the OCT signal, N the total number of consecutive B-scans compared in pairs, i is the i-th B-scan and (x, z) the tomogram coordinates along the fast scan direction and the axial direction, respectively, i.e. the B-scan coordinates; y is the so-called slow scanning direction. Other approaches based on intensity typically work with the variance or correlation between consecutive scans.

2.2.2 Phase-Based OCTA

Similarly, the phase-based OCTA (pOCTA) exploits the argument of the complex OCT signal. Consecutive B-scans are compared calculating the phase difference as follow:

$$\Delta\varphi(x, z)_i = arg\{\exp[-i\varphi(x, z)_{i+1}] \exp[-i\varphi(x, z)_i]\} \tag{2.2}$$

OCTA signal is obtained averaging the phase differences calucated at the same location [5]:

$$I_{pOCTA}(x, y, z) = \frac{1}{N-1} \sum_{i=0}^{N-1} |\Delta\varphi(x, z)_i| \tag{2.3}$$

As mentioned before, pOCTA has an higher sensitivity to noise, specially to sample displacement. Thus, bulk motion correction algorithms are required. The simplest solution is to correct each A-scan by subtracting the circularly averaged phase difference $\overline{\Delta\phi}(x)_i$ from the respective A-scan located at x.

Even if pOCTA requires more corrections respect to an intensity-based approach, in situation of strong back-scattering it's potentially able to provide a better contrast thanks to its intensity indipendency [4].

2.2.3 Complex signal-Based OCTA

The full complex information of the signal can be used as well. Thus, the difference can be applied directly to the complex OCT signal of consecutive scans as follow:

$$I_{cOCTA}(x, y, z) = I_{i+1}(x, z) - I_i(x, z) \tag{2.4}$$

where $I_i(x, z)$ is the complex OCT signal of the i-th B-scan located at y. If this expression is performed with the raw spectral data S before the Fourier transform ($FFT[S(x, k)] = I(x, z)$) it's usually referred as optical micro-angiography (OMAG) but, since the FT is a linear operation, the two formulations are equivalent [6].

Exploiting the full complex information, the advantage respect to pOCTA approaches is the higher sensitivity to blood flowing perpendicular to the sample beam. Also, slow flows that induces only pahse changes will not be detected by an iOCTA approach. Thus, a complex OCTA technique is supposed to lead to better contrast, vessel connectivity and SNR than techniques previously described [6].

2.3 Interscan time and flow velocity

The intensity of the OCTA signal is related to the detection of changes in OCT signal. Typically, a threshold has to be used to discriminate a signal due to background noise from a real flow. However, in order to establish if a flow is detectable or distinguishable from changes in OCT signal, interscan time of the system and blood flow velocity must be taken into account. In the case of interframe scan protocol, the time between two A-scans acquired at the same location is equal to the number of lateral position in one B-scan multiplied by the inverse of the A-scan rate plus the fly-back time. The position and orientation of RBCs within the beam width after this time depends on both interscan time and flow velocity. If the interscan time is short and the RBCs are moving slowly, the cells will be approximately in the same position in both acquisitions, thus the difference in OCT signal could be too low to be detected. On the other hand, if the flow velocity is high, a short interscan time allows to detect a change in OCT signal and also, within a certain range of flow velocities, the intensity of OCTA signal linearly depend on the flow velocity. Therefore, short interscan times are characterized by a poor sensitivity to detect slow flows but it's possible to distinguish high flows. Vice versa, if the interscan time is longer, the sensitivity to slow flows raises but high flows are only detectable and no more distinguishable since the distance travelled by a scatterer during the interscan time is longer than the beam size. Thus, flow velocities above a certain level lead to comparable OCTA signals with fluctuations due only to the amount of scatterers inside the voxels during the scans. Hence, the relation between interscan time and flow velocity is in general linear up to a saturation level that is the fastest distinguishable flow and depends on the the interscan time of the system [7].
A mathematical description of this behavior was provided by Choi et al. [8] and here is briefly summarized. Considering the OCT signal as the sum of the phasors of the reflected light from all the scatterers within the coherence volume, developing Eq. 2.4, the complex OCTA signal can be expressed as:

$$I_{OCTA} = |A(t + \Delta t)e^{i\phi(t+\Delta T)} - A(t)e^{i\phi(t)}| \tag{2.5}$$

where $A(t)$ and $\phi(t)$ are the time-varying amplitude and angle of the the OCT signal expressed as a phasor. With the simplified assumptions of single scattering regime,

reflections modeled by ray optics and equal reflectance of the scatterers in the voxel, the OCT signal amplitude is related to the amount of scatterers N as follow:

$$A(N)^2 = 0.89\alpha(t)\sqrt{N} \qquad N \geq 2 \tag{2.6}$$

where $\alpha(t)$ is the time dependant reflectance of scatteres that depends on the orientation of the scatterer respect to the beam. Without taking into account the noise components in the OCT signal, assuming the scatterers independent with isotropic dynamics and assuming a Gaussian velocity distribution, the OCTA signal can be finally expressed as:

$$I_{OCTA} = \sqrt{[0.89\sqrt{N}(\alpha(t) + \alpha(t + \Delta T)) \left[1 - \left[\exp\left(-\tfrac{8}{6}\left(\tfrac{2\pi}{\lambda_0}\right)^2 \langle V^2 \rangle \Delta T^2\right)\right]^{1/2} \times cos(\Delta\phi(t))\right]} \tag{2.7}$$

where λ_0 is the center wavelength of the OCT light source and $\langle V^2 \rangle$ is the second moment of the velocity distribution. Assuming a spherical shape of the scatterers, it's possible to easily express the number of scatterers N as a function of the scatterer concentration, the voxel volume and the spherical scatterer volume:

$$N = \frac{6C \cdot V_{voxel}}{\pi d^3} \tag{2.8}$$

with d the diameter of a scatterer and C the scatterer concentration. Thus, the simulation of a OCTA signal as a function of the flow velocity for different interscan time ΔT is shown in Fig. 2.2 [8]. It can be observed that, below the saturation level, the range in which the signal-velocity relation is linear highly depends on the interscan time. Considering the physiological capillary blood cell velocities of 0.4 - 0.9 mm/s [9], a proper interscan time can potentially make the OCTA signal able to discriminate capillary flow velocities. Indeed, even if the model is very simple and based on strong assumptions as the single scattering regime or the spherical scatterer shape, it has been shown that the interscan time can be used to detect capillary flow velocity, e.g. in human retina capillaries in order to assess early-stages of retinal diseases [10].

2.4 Advantages and limitations

Among many methods for human skin blood vessel imaging, the main advantage of OCTA lies in being a non-invasively *in vivo* contrast agent-free technique with a penetration depth of about 1-1.5 mm and a resolution down to a few μm. The acquisition time is higher than a structural OCT but nevertheless a scanning time of few seconds is typically required for an area of 1 cm^2. Also, structural OCT data are intrinsically co-registered with OCTA allowing to easily display both information. Since the rapid acquisition time and the protocol without any contrast agent involved, during a single imaging session the OCTA scanning can be repeated multiple times, e.g. to assess microvascular response to functional stimulation.

On the other hand, OCTA is affected by several limitations as well. Firstly, the field of

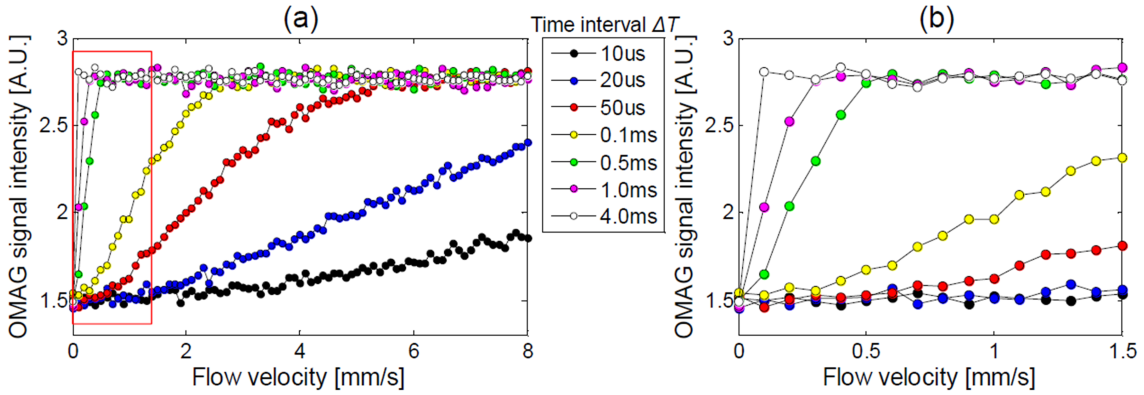

Figure 2.2: (a) Numerical simulation of OMAG magnitude over flow velocities by varying the time interval. (b) A zoom-in view of the red box in (a). Adapted from [8].

view (FOV) is limited by the A-scan rate since bigger volumes required longer times to be acquired. Then, it must be considered that OCTA is capable of highlight the vascular network but not to assess alterations in vascular permeability or leakage as other techniques. OCTA signal quality relies on several choices like the scanning protocol, the algorithm and the OCT system as well. For instance, the OCTA penetration depth is bigger than other methods, such as dermoscopy, but it must be taken into account that its value depends not only on the extent of the vessels but on both intravascular and extravascular tissue since OCTA is obtained through OCT signals processing. Also, considering that human skin thickness can reach 5 mm, OCTA penetration depth is still not enough to visualize deeper plexus and other imaging techniques, such as photoacoustic imaging (PAI), are needed. Furthermore, PAI is able to extract some functional parameters that OCTA cannot, e.g. the oxygen saturation level [11].
Because of the OCT dependency, OCTA is affected by different types of artifacts as well. For instance, the shadow artifacts on OCT has the effect to hide vessels that could be located in depth. Other OCTA artifacts are mainly the projection artifact, due the fluctuating light transmitted by the blood vessels that illuminates the deeper layers and results in a wrong flow detection, and the motion artifact that, especially in vivo, could invalidate sets of B-scans that will appear brighter than the rest of the volume.

3. Skin mimicking optical phantoms

The skin is the largest organ of the human body covering a surface area of about $2m^2$. It's composed of three layers (Fig. 3.1), each with its composition and optical properties as will be described later. The peculiarities of each layer and blood vessels it contains must be obviously taken into account during the design of a skin mimicking phantom.

3.1 Skin and capillaries

The most superficial layer of the skin is the **epidermis**. It is a self-renewing epithelial tissue composed, in turn, of four layers: basal layer, spinous layer, granular cell layer and stratum corneum. Its total thickness depends on different aspects such as age, pigmentation and body site. In average, the epidermal thickness is typically between 60 and 600 μm [12][13].
Beneath the epidermis is the **dermis**, a connective tissue containing nerves, blood and lymphatics vessels. It's composed of two layers, the papillary dermis and the reticular dermis (Fig. 3.1), but without a real distinct boundary between them. The upper surface of the dermis is shaped into numerous papillae forming the dermal-epidermal junction at their interface. The blood flow is supplied to the skin by a system of vessels organized in plexi, three of which are located within the skin thickness: at the junction of the papillary and reticular layers there is the subpapillary plexus from which small capillaries branch out forming one perpendicular capillary loop per papillae; in the middle part of the dermis there is the reticular dermal plexus, mainly venous; finally, in the deepest portion of the reticular dermis there is the deep dermal plexus [14]. In average, the thickness of the dermis is typically between 1 and 4 mm [12][13].
Lastly, the **hypodermis** or subcutaneous tissue is an adipose layer helping in thermal insulation, shock absorbing and storing of metabolic energy. Also, especially in the deeper portion of this layer, it contains the main trunks of subcutaneous nerves, vessels and lymphatics. The hypodermis thickness is typically between 5 and 20 mm [12][13], depending on the location.

The microcirculatory system consists of three types of microvessels: arterioles, capillaries, and venules. Arterioles take blood from arteries and supply it to the capillaries where leaky vessel walls allow to exchange substances; from the capillaries, blood flows then to the venules. Capillaries are organized in the so-called capillary beds and are distributed inside the skin in quantities of about 16-65 capillaries per mm^2. Arterioles

and veins are characterized by a diameter of 10–100 μm and 10-200 μm, respectively, and they're both innervated so that the layer of smooth muscle cells surrounding them can control vasoconstriction and vasodilation to regulate blood flow and pressure. On the contrary, capillaries are typically 8–10 μm in diameter, not innervated and not surrounded by muscle cells [15][13].
At the capillary level, the average red blood cells velocity is about 0.84±0.53 mm/s in the arteriolar limb and 0.47±0.29 mm/s in the venular limb [16].

However, the anatomy and function of healthy peripheral vascular systems may differ in subject affected by vascular diseases, depending also on the severity. Venous diseases, in particular, attracted more interest because of the higher prevalence and the impact to the quality of life for most severe conditions. If venous system diseases are relative to the lower extremities and associated to conditions of high venous pressure and venous reflux, they are referred to as **Chronic Venous Insufficiency** (CVI). From a clinical classification point of view, seven classes describe CVI, from absence of symptoms up to active ulcer. The intermediate stages are typically characterized by different levels of dilation, elongation and tortuosity of capillary beds as well as thickening of basement membranes [17]. Non-invasive imaging techniques play a key in role in CVI diagnosis.
CVI vasculature features were taken into account during this work to develop pathological morphology mimicking vessels.

Considering the few millimeters of penetration depth of an OCT system, the skin layers that can be investigated by this technology are dermis and epidermis, thus OCTA can mainly investigate the the microvasculature of more superficial plexus.
Since the different composition of these layers, the interaction between the layers and the light changes and it can be described by some coefficients, as described in the next section.

3.1.1 Optical characteristics

In order to characterize the skin layers from an optical point of view, some parameters that describe the interaction of matter with light must be taken into account. Typically, they are wavelength dependent parameters. The most important ones are reported below.

The **refractive index**, n, is the ratio of the light speed in vacuum to that in the medium of interest. Its value affects the path of reflected light entering or leaving the medium. The skin has a refractive index around 1.4, but it can slightly vary depending on skin moisture.
The **absorption coefficient**, μ_a (mm^{-1}), describes the rate of decrease in light intensity into a medium due to absorption. Thus, it's a measure of light penetration depth only related to the amount of photons absorbed per distance inside the medium that convert light energy. The μ_a values characterizing dermis and epidermis for a wave-

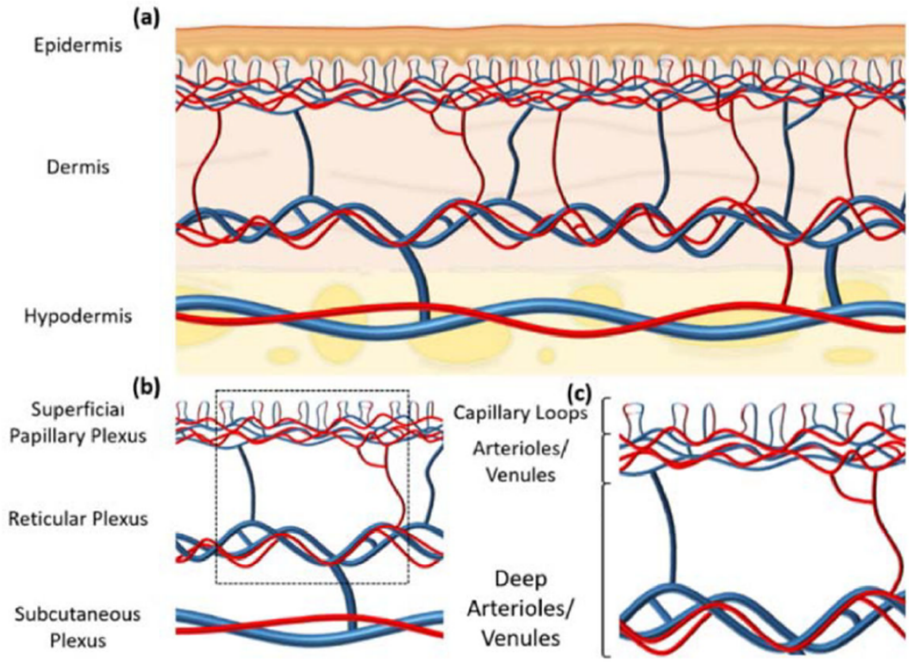

Figure 3.1: Cutaneous vasculature. (a) Healthy skin divided into the three primary layers: the epidermis, the dermis, and the hypodermis. (b) Vasculature of healthy skin. The black square highlights the vessels that canbe mainly imaged by cutaneous imaging modalities. (c) Zoom of the black square in (b). Adapted from[13]]

length of 1300 nm are collected in Tab.3.1 [18].
The **scattering coefficient**, μ_s, is a measure of the amount of photons scattered by the medium per distance. Scattering can occur over all possible directions. However, since the scattering is typically not isotropic, it's useful to consider the directionality of it. Indeed, the scattering is commonly expressed in terms of **reduced scattering coefficient**, μ'_s (mm^{-1}), obtained through the anisotropy factor, g, as follow:

$$\mu'_s = \mu_s(1 - g) \tag{3.1}$$

The anisotropy factor is the average value of the cosine of the scattering angle over the scattering pattern, or probability. It means that for an isotropic scattering, g is equal to zero. If the pattern is anisotropic, the idea is to split it into an isotropic component, with g equal to zero, and an anisotropic one characterized by g. Thus, the new isotropic component has to be weighed as $1 - g$ and it's then referred to as "reduced" scattering. Considering the reduced scattering step size, $1/\mu'_s$, the reduced scattering coefficient is a measure of the diffusion of photons in a random walk with that step size where each step involves isotropic scattering. The μ'_s values characterizing dermis and epidermis for a wavelength of 1300 nm are collected in Tab.3.1 [18].

@1300 nm	$\mu_a(mm^{-1})$	$\mu'_s(mm^{-1})$
Epidermis	0.078	2.53
Dermis	0.12	1.61

Table 3.1 Absorption and reduced scattering coefficients for epidermis and dermis at 1300 nm light wavelength [18].

3.2 Skin optical phantoms state of art

Standard test methods and optical phantoms have been required because markets of OCT and OCTA are still growing. Specifically, in the field of ophthalmology, it is necessary to prove the image quality and performance for accurate disease diagnosis. In addition, when a system is evaluated, or quality assurance and software modifications are conducted, experiments with human or animal eyes should be performed. However, preclinical and clinical trials cannot be carried out frequently, and it is difficult to obtain reliable and consistent data for system validations. Additionally, it is difficult to obtain subject-independent data. Therefore, a retinal phantom for OCT and OCTA, which ameliorates these problems, is thus needed.

Tissue-simulating phantoms are crucial in the development of optical imaging techniques, such as OCT, in order to validate physical models or simulations, testing and optimizing the system, evaluating repeatability and reproducibility as well as comparing performance between different systems on standardized samples [19]. Even if the characteristics of the phantom depend on the specific application, there are some generic properties that an "ideal" skin phantom should have [19][20]:

- Ability to provide optical wavelength dependant tissue-like properties, as well as other properties depending on the application;
- Tunability of properties to mimic different tissue types;
- Stability of properties over time and in various environmental conditions;
- Architectural flexibility (multi-layer morphology, molecules of interest inclusions, mimicking tumors inclusions...) ;
- Ability to incorporate realistic perfusable structures to mimic blood flow;
- Simple and reproducible preparation;
- Low maintenance in terms of storage and transport;
- Safe to prepare and handle;
- Recipe characterized by easily available, low-cost ingredients and standard fabrication equipment;

3.2.1 Bulk materials and additives

Many materials have been investigated for tissue-mimicking phantoms development, mainly aqueous suspensions, hydrogels, resins, PVCP and silicone, in particular PDMS.

Aqueous suspension phantoms are used in optical imaging specially because of the simple and cost-effective preparation. Skin optical properties can be easily matched using, for instance, fat emulsions or microspheres for scattering and ink for absorption. The results are versatile, since the optical properties can be easily modified tuning the dilution rates, but at the same time are highly reproducible. A typical example is Intralipid, a stable emulsion of soybean oil, egg yolk phospholipids, glycerin and water.
Some disadvantages limit the applications of this type of phantoms, characterized by a poor stability over time (the shelf life is tipically of a few hours to days), low architectural flexibility and possible artefacts from the container walls [20].

Better results in terms of architectural flexibility are achievable through hydrogels, cross-linked polymer networks that are swollen by water and made from either natural or synthetic sources. Agarose and gelatin are broadly used but still suffer from poor stability over time, in addition to complex storage due to dehydration, bacterial ingrowth and possible damages [20].
For better stability, poly(vinyl alcohol) cryogel (PVA-C) can be used [21]. PVA is dissolved, typically in water, obtaining a liquid hydrogel that then cross-link alternating freezing and thawing cycles. The number of freeze/thaw clycles (FTCs), as well as the solvent and the additives, defines the optical properties of the material. However, the preparation is critical and reproducibility could be an issue. Also, the long-term stability relies on hydrated storage in sealed containers [22].

Differently from the previous ones, phantoms insoluble in water simplify the maintenance phase, have a longer shelf life and allow to obtain more realistic morphology, such as a multilayer skin phantom. Between them, PVCP, polyvinyl chloride-plastisol, is a white opaque suspension of PVC resin in a liquid plasticizer that becomes transparent if heated. For absorption coefficient tuning, pigment-based absorbers are commonly used as well as TiO_2 for scattering coeffient [23]. However, PVCP toxicity due to phthalates based plasticizers can be an issue.

Another non-water-based-material use for tissue-mimicking phantom is resin. Polyurethane is a transparent solid mix of a resin and a hardener. It's characterized by short hardening times, long stability and optical properties tunability typically adding microspheres or metal oxides powders for scattering and pigments, inks or carbon powders for absorption. TiO_2 and India ink are often used [24]. Toxicity must be still taken into account because of the possible presence of unreacted ingredients such as isocyanates [20].

Finally, a widely used material for mimicking tissue is silicone. It's typically available into kits composed of a base material and a hardener that cures the silicone at

room temperature or faster at higher temperatures. The silicone matrix can incorporate several inorganic additives for scattering and absorption properties with high stability. Vacuum degassing is typically needed to obtain homogeneity. During the last years, polydimethylsiloxane (PDMS), has been widely utilized for tissue-mimicking phantoms specially because of its stability, easy handling, excellent architectural flexibility and the achievable optical, mechanical and thermal properties. PDMS refractive index is typically between 1.40 and 1.44, making it particularly suitable for matching skin behavior. The most used additives for scattering and absorption coefficients matching are metal oxides particles, silicone pigments, inks and dyes. For instance, independent control of absorption and scattering coefficients by separately tuning the concentration of carbon black powder (CBP) or titanium dioxide powder (TDP), respectively, has been demonstrated [25].

3.2.2 Micro-vasculature embedding

One of the crucial features of a skin phantom, especially for OCTA applications, is the possibility to perfuse it with blood or a blood-mimicking fluid. Several approaches have been developed during years with different degree of morphology truthfulness and simplicity of preparation. The compromise between them depends on the application. Here, the most used and the most innovative techniques are reported as well as some relevant example of recent proposed approaches in literature.

Starting from the simpler techniques, copper wires could be used as mold for a channel simply surrounding them with the bulk material when it is in the softest form. Then, after the hardening phase, the copper wire can be removed leaving an hollow path for perfusion. Similar approaches are fast and easy to reproduce but only simple morphologies can be obtained. In Fig. 3.2A is shown the example of the development of straight and slightly tilted straight channels with a 200 μm copper wire embedded into a PVA cryogel [21] while in Fig. 3.2B is shown a more complex structure made with copper wires tree that, thanks to the high elasticity of the PVCP used as bulk material, can be removed without compromising the structure integrity [23]. Also, simply depositing a epoxy resin drop on the wire, is possible to mimic aneurysms.
From these example, it's clear that such results are limited in terms of shape complexity and it's difficult obtaining not linear paths. Also, the bulk material above the channels must be thick enough to ensure the integrity of the structure after wire removal.

An approach capable of obtaining more customized shapes through copper mold is shown in Fig. 3.2C [24]. A specially designed and cut copper mould is embedded between two polyurethane (PU) slabs containing TiO_2 and India ink. Two holes on one of the two slabs allow the contact between the copper mould and an electrolysis pool that dissolves the copper releasing the hollow path for perfusion. However, the unrealistic result, consisting of a model lying on plane surface, is still a limit.

During the last years, the development of realistic tissue-mimicking phantoms has been

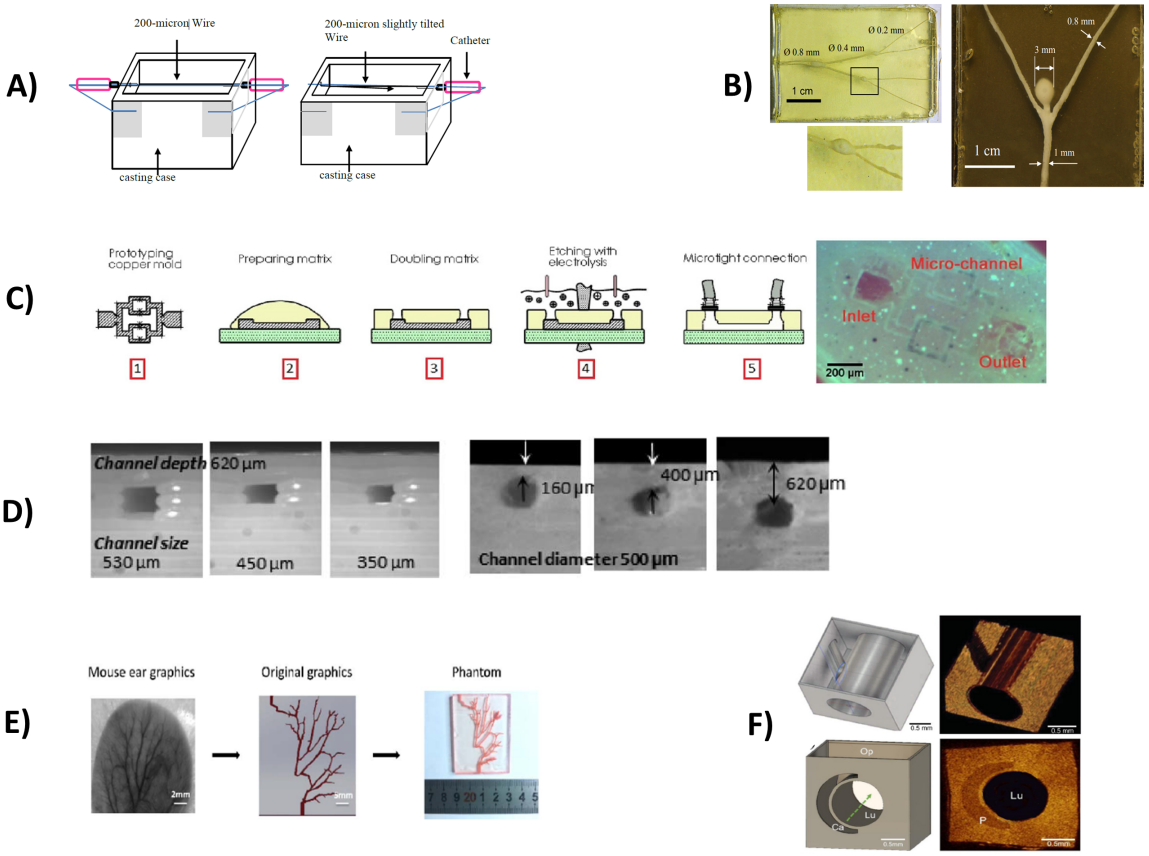

Figure 3.2: Phantom developing approaches from literature. (A) Copper wire mold for straight channels [21]. (B) Copper wire mold with branches and aneurysm [23]. (C) Combination of copper network mold and electrolysis [24]. (D) Channels obtained with 3D-printers based on thermosoftening and photopolymerization [26]. (E) Combination of spin coating and DLP printing for multi-layers phantom [27]. (F) 2PP 3D-printed scaffolds filled with PDMS mixture for IVOCT applications [28].

supported by 3D-printing techniques implementation. Both indirect printing of phantom moulds or direct printing of bulk materials previously mixed with additives has been used [20]. However, the available materials for 3D-printing may be not suitable for properties tuning and proper characterizations are needed.
Different 3D-printings techniques has been demonstrated to be a potential method for phantom fabrication. For instance, printers based on thermosoftening and photopolymerization have been tested, obtaining channel size down to 0.35 mm (265 $\pm$ 5 μm of layer thickness) and 0.2 mm (28 μm of layer thickness), respectively (Fig. 3.2D) [26]. Three different polymers were used: ABS, an inexpensive and resistant thermoplastic polymer for thermosoftening printing and two photopolymers characterized by low and high turbidity for the photopolymerization printing. Their optical properties were measured over a wide wavelength range finding the need to incorporating chromophores or scatterers depending on the wavelength of interest.

An example of 3D-printing based approach capable of mimicking both blood perfusion and skin optical properties and morphology is shown in Fig. 3.2E [27]. It's a three layer phantom, composed of a 30 μm layer to mimic epidermis and a 200 μm layer to mimic dermis, both fabricated by spin-coating of a mixture of PDMS, India ink and TiO_2, and a 3 mm layer to mimic hypodermis that contains a 3D vascular model of 1 mm in diameter fabricated by digital light process (DLP) printing using a photoreactive resin as base material. This approach yields a quite realistic and customized result but the optical characterization is provided only for the PDMS layers and not for the resin in which the vascular network is embedded. Also, only the bigger vessels of the hypodermis are mimicked and not smaller structures such as the capillaries of few micrometers in diameter located in the papillary loops.

Finally, a recent approach mainly focused on intravascular OCT (IVOCT) highlights how 3D-printing and in particular the two photon polymerization (2PP) printing can be used to create scaffolds for anatomical structures with relevant features at the microscopic scale [28]. Indeed, as will be discussed below, 2PP printing enables printing with resolutions down to few micrometers or even hundreds of nanometers depending on the photoresist. Thus, scaffolds with high fidelity vascular structures can be printed using a photoresist that is largely transparent at the considered size scales and then microinjection can be used to fill the scaffold with **any** tissue-mimicking material, in this case a mixture of PDMS and TiO_2. In Fig. 3.2 F are reported two results from that study. The first one is a scaffold with a main channel of 1 mm in diameter to insert the IVOCT imaging probe and a side branch of 600 μm in diameter; the scaffold was then filled with the PDMS mixture. The second model is a scaffold with a main channel and a separate arc-cavity independently filled with lipid inclusion to mimic an arterial plaque. Considering the 2PP printer resolution, vessels with diameter down to the capillary size can be printed.

3.2.3 Two-photon polymerization 3D-printing

Two-photon absorption (TPA) is a theory, first predicted by Goeppert-Mayer in 1931, that describes the phenomena of a molecule simultaneously absorbing two photons, with equal or different energies, to reach the excited state from the ground state. If the photons have the same energy, then the probability that TPA occurs depends on the square of the excitation laser intensity. If the two photons have different energies, the TPA probability depends on the product of the two excitation lasers intensities. Thus, the maximum TPA absorption is localized in the vicinity of the laser beam focal point, i.e. where the TPA probability is higher [29].

Two-photon polymerization (2PP) 3D-printing exploits the TPA theory to print submicrometer resolution structure from photosensitive materials using a focused laser beam instead of a photomask. Thus, the laser beam focal point defines the printing voxel volume and the printing process is performed voxel-by-voxel with a resolution down to few hundreds nanometers. The photoresist used for 2PP 3D printing can be

negative or positive. In the first case, the exposed polymer-chains are cross-linked and the unexposed ones are washed out. Viceversa, with a positive photoresist the TPA induces chain scission, softening the resin that can be dissolved and then washed out [30]. In Fig. 3.3 is represented the 2PP 3D-printing in "vat" mode, i.e. with the object extracted from the photoresin vat as it's printed.

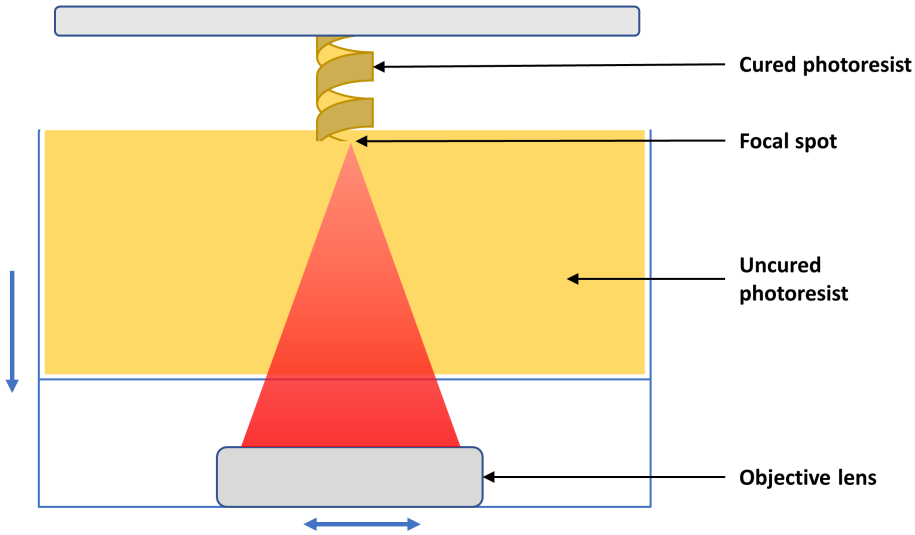

Figure 3.3: Diagram of a 2PP printer in "vat" mode. Here is represented a positive photoresist.

A generic 2PP printing set up typically involves a femtosecond laser, microscope objective lens to focus the laser beam into the desired voxel, a mirror scanner system or linear stage for x-y-z movements and a camera for on-line monitoring.
The printing resolution depends mostly on the power of the laser involved and on the exposure time that, in turn, depends on the efficiency of 2PP initiators.

3.3 Employed approach

The work described in this thesis is the development and extension of a project born at the *Center for Medical Physics and Biomedical Engineering* (*Medical University of Vienna*) by *Leitgeb* & *OC-PAI* research group.

The idea was to propose a multi-layer optical skin mimicking phantom for multi-modal imaging, capable of mimicking the morphology and optical properties of dermis and epidermis, with realistic embedded perfusable microvasculature representative of healthy and pathological morphologies.
The vessels are modelled starting from real acquisitions on both healthy and pathological subjects, allowing to obtain realistic structures and realistic flow velocity distributions as well. The 2PP 3D printer is capable to directly printing the hollow vessel with an adjustable wall thickness and with a resolution of few micrometers, enabling vessels

with inner diameters down to about 8 μm to be printed. An external vat enables to connect the vessel to a needle for perfusion and to embed the vessel into two different layers of PDMS. Adding black and white pigments into the PDMS, the optical properties of dermis and epidermis can be properly mimicked. The result of this approach is a highly realistic phantom, with a vessel easy to customize and a standardized recipe relatively easy to reproduce.
During this work, the investigated imaging technique was mainly the OCTA but, considering the morphology, composition and dimension of the developed phantoms, they represent a potential standardized way to test and evaluate other imaging techniques, such as photoacoustic imaging (PAI).

The details of methods and results are reported in the next chapters.

Part II

Materials and Methods

4. Employed OCT system and OCTA algorithm

The work described in this thesis was carried out at the *Center for Medical Physics and Biomedical Engineering* (*Medical University of Vienna*), in collaboration with the *OC-PAI* research group. The available OCT system and scanning protocol are then described in this chapter together with the implemented data processing.

4.1 OCT system

The employed OCT system is a custom-built fiber-based OCT system based on an akinetic swept-source (Insight Photonic Solutions, USA). It's characterized by a central wavelength of 1300 nm, a bandwidth of 30 nm, and a power of 60 mW. However, part of the power is lost before hitting the sample and less than 20 mW reach the target.
The laser has a Duty Cycle of 100%. It means that the laser continuously sweeps over the bandwidth range without waiting for the laser to switch to the next location. Thus, alternately, one complete sweeping cycle is saved and the next one is skipped so that the time needed for the skipped cycle can be used to align the laser on the next location. However, this solution is applied only when the OCTA scanning protocol is utilized and not for the OCT acquisitions for which all the sweeping cycles are taken into account.

The system is summarized in Fig. 4.1 [31]. A fiber coupler splits the source beam into reference arm (25% of the power) and sample arm(75% of the power) where a rotatable imaging probe and a system of lens allow to obtain a flat imaging plane. The beams are then recombined by 50/50% fiber coupler and a dual balance detector records the cross-correlation term.
The scanning of the volume, i.e. the switching of the laser lateral position, is performed by two scanning galvanometers. The A-scan rate of the system is 222.22 kHz.

The lateral and axial resolutions are 31.5 μm and 22 μm in air, respectively, while the axial and lateral pixel size are 13.3 μm and 19.6 μm, respectively. However, in order to obtain the correct value of axial pixel size, when a sample different from air is imaged, the axial pixel size is divided by the refractive index of the sample. Then, considering the average refractive index for skin of 1.4, the resulting axial pixel size is 9.5 μm. About the lateral pixel size, that value is referred to an "OCTA mode" acqui-

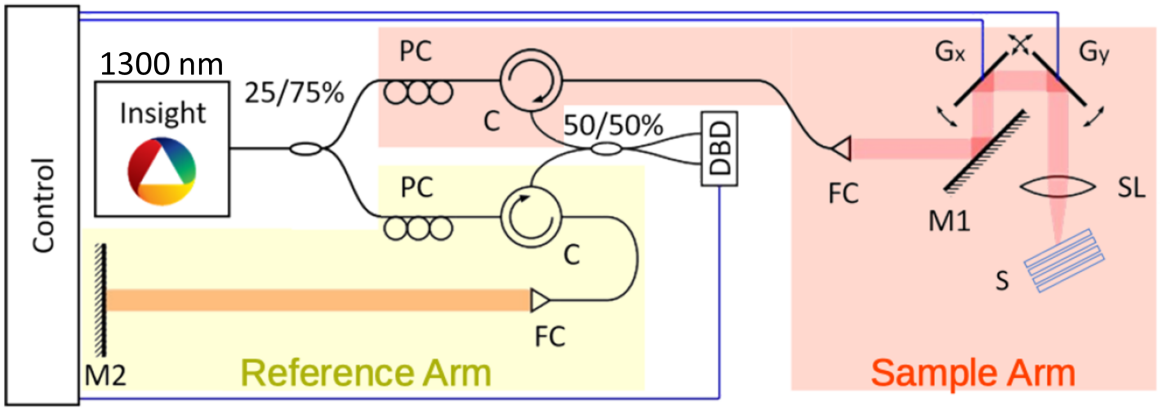

Figure 4.1: OCT setup. PC: polarization control; C: circulator; FC: fiber collimator; M1, M2: mirrors; Gx, Gy: scanning galvanometers; SL: scan lens; S: sample; DBD: dual-balance detector. Adapted from [31].

sition; when the "OCT mode" is selected, since not any sweeping cycle is discarded, the lateral resolution is halved.

4.2 Scanning protocol and Data format

The "OCTA acquisition mode" of the employed OCT system utilizes a BM-scan protocol. It means that the acquisition of a B-scan is repeated multiple times at the same location before switching to the next location for a number of times equal to the number of OCT volumes that will be used to extract the angiography.
In the standard protocol, the system was set to acquire 4 volumes with 512 B-scans per volume, 512 A-scans per B-scan and 2176 pixel per A-scan. Actually, not all the 2176 pixel in depth will be valid. After each laser calibration, because of the transition between valid sweep sub-intervals, a list with only valid data points is provided.
The A-scan rate of the system is 222.22 kHz, thus the interscan time between consecutive B-scan can be calculated as the number of A-lines per B-scan multiplied by the time to acquire a single A-scan, i.e. 4.5 µs. Actually, even if the acquired volume has 512 A-lines per B-scan, the real number of A-scan position is 1024 and then, alternately, one A-line is saved and the next one is discarded. Thus, the real interscan time is obtained as 4.5 µs * 1024 = 4.6 ms. Actually, the flyback time of the laser should be also taken into account. It's not known but was roughly calculated to be less than 1 ms.
The data are organized in 32 files, each containing the raw spectral data of 64 B-scans i.e. the 4 B-scans from 16 different lateral positions, for a total of 32768 A-lines.

When the "OCT acquisition mode" is set, only one raster scanning of the volume is performed. In this acquisition mode, only one volume is acquired but all the 1024

A-lines composing a B-scan are taken into account. Then, the amount of data is only halved and the A-scans are organized in 16 files, each containing the same amount of A-lines as before, i.e. 32 B-scans.

The FOV obtained with the standard protocol is 10 mm x 10 mm. Depending on the experiment, the protocol was changed in terms of number of A-scans per B-scan and field of view obtaining different interscan times.

4.3 Reconstruction algorithm

The reconstruction algorithm can be divided into two steps. The first one is the OCT signal extraction from the raw spectral data. Then, the OCT signal is processed in order to extract the angiography. Both reconstructions were made with Matlab.

OCT extraction

The OCT reconstruction is essentially based on an already existing Matlab code that was adapted to suit the specific data to be processed depending on the protocol used in the experiments.
Firstly, the raw spectral data are loaded file by file and organized in A-lines. Then, for each A-line, the first step is to discard the data from invalid points according to the calibration output.

Then, the background subtraction is performed. It can be done in two ways, also depending on the type of data to be processed.
On the full volume acquisitions, the average A-line was extracted for each lateral location, i.e four groups of 4 B-scans. Then, it was subtracted from each A-line acquired at that lateral location.
In some experiments, the same A-line was repeatedly acquired. Then, for a proper background subtraction it was necessary to block the sample arm, acquire the background data-set, perform the average of each depth obtaining the averaged background A-line and then subtract it from each A-line of the volume.

Before applying the Fourier transform, zero padding was applied to each signal to increase the number of points per signal. Also, when artifacts were too evident, signals were windowed using a Gaussian window. In this way, even if a decrease in resolution occurs, reflections artifacts are significantly reduced.
Then, the Fourier Transfrom was finally applied and the symmetric spectral copy was removed.

If the "OCT acquisition mode" was set, then the OCT complex signal is ready and both magnitude and phase information can be exploited.

$$FFT[S(x,k)] = I(x,z) = A(x,z)exp[-\phi(x,z)] \tag{4.1}$$

Typically, the magnitude is extracted and then the images are shown in a logarithmic scale.
Otherwise, if the "OCTA acquisition mode" was used, the four OCT volumes must be properly separated so that, depending on the algorithm, they can be compared to extract the OCTA volume as described below.

When the OCT images are shown, pixels with value below a certain threshold are typically set to zero so that the contrast is improved. The threshold depends on the volume and was empirically found in terms of percentage of the brightest pixel. Also, if necessary, Wiener filtering was applied for noise attenuation.

OCTA extraction

Starting from the four complex OCT volumes, one complex signal-based and two intensity-based OCTA signal algorithms were mainly implemented, depending on the experiment.

The complex-based OCTA was mainly implemented during OCTA signal characterization on a simple tube and not on the phantom since the phase information is more critical to exploit. Since the reference model for OCTA signal was based on OMAG signal [8], the cOCTA was obtained as follow:

$$cOCTA_{OMAG}(x,y,z) = \frac{1}{N-1}\sum_{i=1}^{N-1}|I_{i+1}(x,z) - I_i(x,z)| \tag{4.2}$$

where I is the complex OCT signal.
The main intensity-based technique used in this work is the averaging of differences bewtween pairs of consecutive logarithmically-scaled intensity scans [5]:

$$iOCTA_{log}(x,y,z) = \frac{1}{N-1}\sum_{i=1}^{N-1}|log(A_{i+1}(x,z)) - log(A_i(x,z))| \tag{4.3}$$

where A is the OCT signal intensity.
Then, because of a better noise reduction from the background that helped during angiography segmentation, the full-spectrum decorrelation based on signal amplitude was also applied [32]:

$$iOCTA_{dec}(x,y,z) = 1 - \frac{1}{N-1}\sum_{n=1}^{N-1}\frac{A_n(x,z)A_{n+1}(x,z)}{[\frac{1}{2}A_n(x,z)^2 + \frac{1}{2}A_{n+1}(x,z)^2]} \tag{4.4}$$

The OCTA algorithms performances are in general affected by both multiplicative and additive noise so that, even if two voxels should be characterized by the same OCTA value, the resulting values are different because of noisy OCT volumes. To attenuate the additive noise, a Wiener filtering with a 3x3 window was applied on each B-scan of

the OCT volumes before OCTA extraction. Wiener filter is a 2D adaptive filter that smooths the image depending on the local variance. Then, after OCTA extraction, a threshold was empirically found and applied to remove residual noise. Because of the properties of the logarithmic scale, multiplicative noise should be attenuated when the logarithmic iOCTA is used and additive noise is then removed.

5. Phantom development

Based on previous studies carried on by the *OC-PAI* research group (MUW), the general steps of the phantom development process were defined in order to mimic optical properties of skin, morphology of capillaries and blood perfusion in the best possible way. Also, easier fabrication techniques are preferable so that the proposed recipe could be replicated to obtain standardized skin phantom for OCTA applications.

The proposed approach consists of three main steps. The first one is the design of a realistic vasculature, typically obtained starting from real acquisitions. Then, the second step is the 3D-printinf of the vessels walls merged with an external vat, specially modeled to connect the channel with inlet/outlet holes and to be able to surround the channel with a tissue mimicking material as well. About that, the third step is the preparation, pouring and curing of two different layers of the tissue mimicking material inside the vat to reproduce the optical properties of dermis and epidermis. The details are reported in the following sections.

5.1 Design of the vessel

During this work, different phantoms were printed in order to obtain the best compromise between a realistic vessel and fabrication feasibility and to test the OCTA system skills as well.
In general, two modelling methods were used depending on the purpose the new phantom needed to be printed for. During preliminary tests for OCT and OCTA experiments as well as for printing evaluations, there wasn't the need to have complex and realistic structures. Indeed, in this initial tests, it was easier working with simpler structures and with known diameters. Based on these needs, some vessels were modelled completely from scratch as straight channels with fixed diameters. Afterwards, further printings were made in order to get as close as possible to a real structure, both in terms of shapes and diameters. In this case, modelling the vessel from scratch would have lead to unrealistic results. Thus, it was considered appropriate starting from segmentation of real vascular networks. In particular, all the healthy models obtained with this method came from the segmentation of a thumb vasculature network provided by the Department of Anatomy (MUW) and further processed with *Amira* software. The segmentation was already divided into two labels: arterioles and venules. However, the venous network was very dense and its printability would have been very challenging. Thus, only the arterioles were taken into account. Regarding the pathological mod-

els, they were extracted from an OCT angiography volume acquired on the lower leg of a C4c CVI patient at the *Center for Medical Physics and Biomedical Engineering* (MUW). Both these vasculature volumes are shown in Fig. 5.1. Also, the pathological model was used as a starting point to design a capillary network phantom as well.
The general modeling process consisted then in selecting one vessel, processing and simplifying its morphology, "cleaning" its structure from incomplete bifurcations and smoothing its final surface.

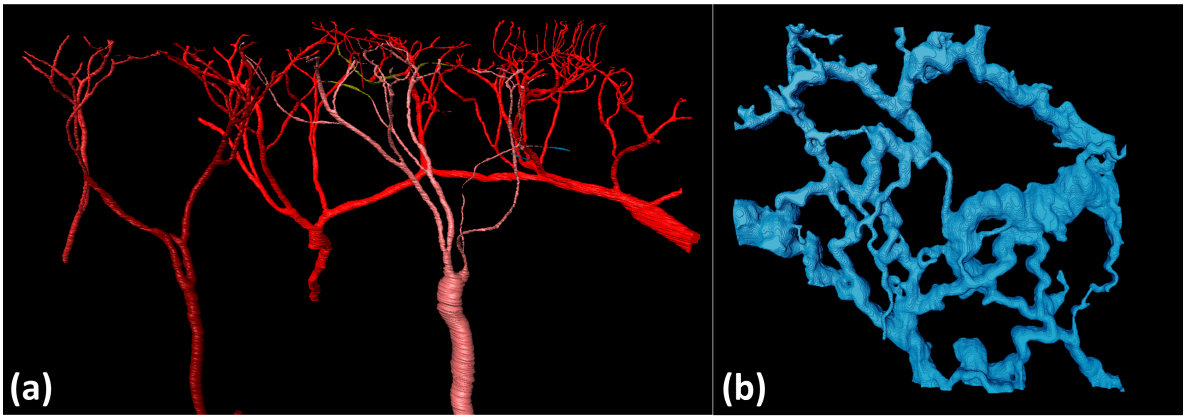

Figure 5.1: 3D vasculature models used for 3D phantom modelling. (a) Healthy thumb vasculature network. (b) Lower leg vasculature of a C4c CVI patient.

Both the modelling methods described above refer to the design of the internal lumen of the vessel. From a printing point of view, the model of the internal lumen defines the hollow surface on which the vessel wall thickness is added. In this way, a realistic and complex structure with an adjustable wall thickness can be printed. As described in the next section, the model of the vessel is then merged with the model of the external vat through the inlet and outlets of the vessel. It means that the vessel is suspended so that later it can be surrounded by a tissue mimicking material. The main risk of this approach is that the suspended structure could collapse under its own weight. In order to avoid it, the length of the vessel must be kept below few millimeters and the wall thickness must be thick enough to sustain all the structure. The wall thickness is actually a challenging parameter: from the printability point of view it's preferable to have thicker walls but from the OCT imaging point of view it must be taken into account that the walls don't yield signal and appear black in contrast to the skin mimicking material. In order to avoid an high contrast between the skin and the walls, the wall thickness should be chosen as the best compromise between these two needs. Thus, the thinnest value capable of supporting the structure must be selected. All the phantom developed during this work are characterize by a wall thickness of 20 μm. A thickness of 16 μm was tested and a leakage was observed.

5.2 3D-printed vat

As mentioned before, the external vat was specially modeled so that the channel could be connected to the inlet/outlet holes where the needles are inserted. In this way, using syringes connected to the holes, a scattering fluid can flow inside the channel during OCTA acquisition. If needles are inserted in both holes, the direction of the flow can be reversed. For this reason, "inlet hole" and "outlet hole" are interchangeable terms and they depend on the specific set-up. Usually, the inlet hole was chosen so that the fluid can flow from smaller to bigger diameter: in this way, dust or agglomerates blocking the channel occurs less frequently.

In Fig. 5.2 a top and side view of the vat with the internal structures are shown. Starting from the left, the inlet hole has a diameter of 0.85 mm where a 0.8 mm needle is inserted and then fixed with glue, paying attention in dropping the glue only on the border and not inside the vat. The tip of the needle was sharpened and then compressed air was used to clean it before use. The path that originates from the inlet hole leads to the fluid collection chamber, a cylinder with the aim to link the path from the inlet hole with the inlet of the vessel. At the right of the vat there is the same structure just described but mirrored to work as the outlet section. Between the inlet and outlet sections there is a cavity where the suspended vessel is located and later the tissue mimicking material will be poured. The model structure has an overall standard dimension of $8 \times 4 \times 2.5$ mm that can be easily modified depending on the needs. Thus, this model was merged with the one of the vessel that has to be printed so that the inlet of the vessel internal lumen comes out from the inlet collection chamber and the outlet of the vessel internal lumen enters into the outlet collection chamber.

The 3D modelling of the vat and the 2PP 3D-printing have been achieved thanks to the effort of the *Additive manufacturing Lab* (MUW).
The resin structures of the phantom, i.e. the vat merged with the vessels models, were printed using the high-resolution two-photon polymerisation (2PP) printer *NanoOne* (UpNano GmbH, Vienna, Austria). Structuring of the models was mostly done with a 5x or 10x objective (Olympus, Tokio, Japan), except for the capillary network that was also tested with the 20x objective. Besides the magnification objective, the resin and the *fine* or *coarse* printing profiles also influence both the axial and tranversal printing resolutions. All the geometries were printed with upphoto (2-photon resin, UpNano) in *vat mode*: it means that a vat is placed above the objective and the printed object is drawn up out of the material vat. Then, the achievable transversal and axial resolutions range from 8 μm and 10 μm, respectively, down to to 0.3 μm and 2 μm, depending on the objective. Also, the actual dimensions of the hollow printed paths depend on the printing "slice mode": with the *simple* mode a voxel is polymerized if at least the 50% of its volume is occupied by the object in the stl file; the *conservative* mode leads to the polymerization of each voxel which volume is not totally empty, independently on the percentage; with the *voxel* mode a voxel is printed only if the 100% of its volume is full. Thus, the *voxel* mode is the one that allows to obtain the maximum dimension of the lumen.

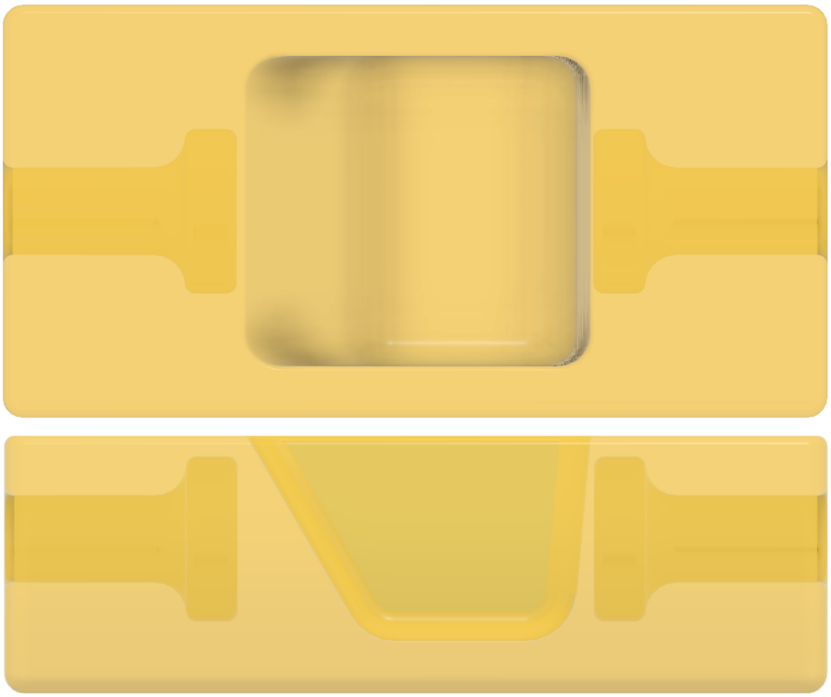

Figure 5.2: Top and side view of the vat. On the left and right sides there are the paths for needles inserting and fixing. In the middle part there is the cavity where PDMS mixtures will be poured. The vessels models are located in the central cavity of this model and merged creating a close path towards the needles.

After printing, the structures were rinsed in isopropyl alcohol and air-dried. Also, in order to remove the uncured resin inside the channel as well, it was necessary to let isopropyl alcohol flow inside the structure. This process must last only few minutes. Otherwise, the cured resin as well would have become softer modifying the shape of the vessel.

5.3 Casting materials

The recipe for skin mimicking materials preparation essentially includes the mix of PDMS (Sylgard™ 184 Silicone Elastomer Kit, *Dow*) and additives, in particular two silicone color pigments (Silc Pig™, *Smooth-On*): the black pigment mostly affects the absorption properties and the white pigment the scattering ones.
Even if only a very small amount of material was needed to fill the vat, since the chosen additives mass percentages are very low, a mass of 10 g of PDMS base material was used for each preparation in order to make the weighing of pigments easier. 10 g of PDMS base material were then mixed with the curing agent supplied in the kit using a weight ratio of 10:1. The pot life at room temperature of Sylgard 184 is 2h so, even if the curing process begins as soon as the two components are mixed, it doesn't affect the few next steps before baking and rather the increase of viscosity help to prevent

from additives sedimentation. The mixture of base material and curing agent was then carefully mixed with the desired weight percentages of black and white pigments until the sample mixture colour appeared homogeneous. In order to remove all the air trapped during mixing, the sample was placed in a vacuum chamber for about 20 minutes, checking that no more air bubbles came out from the sample before ending the process. Finally, the mixture was poured into the vat or, in some cases, into a Petri dish when particular material characterization tests were needed. In order to complete the curing process, the sample could be left at room temperature for 24 h. However, to speed up the process, it was usually baked at 100 °C for 1h as indicated in the data sheet. The process is summarized in Fig. 5.3.

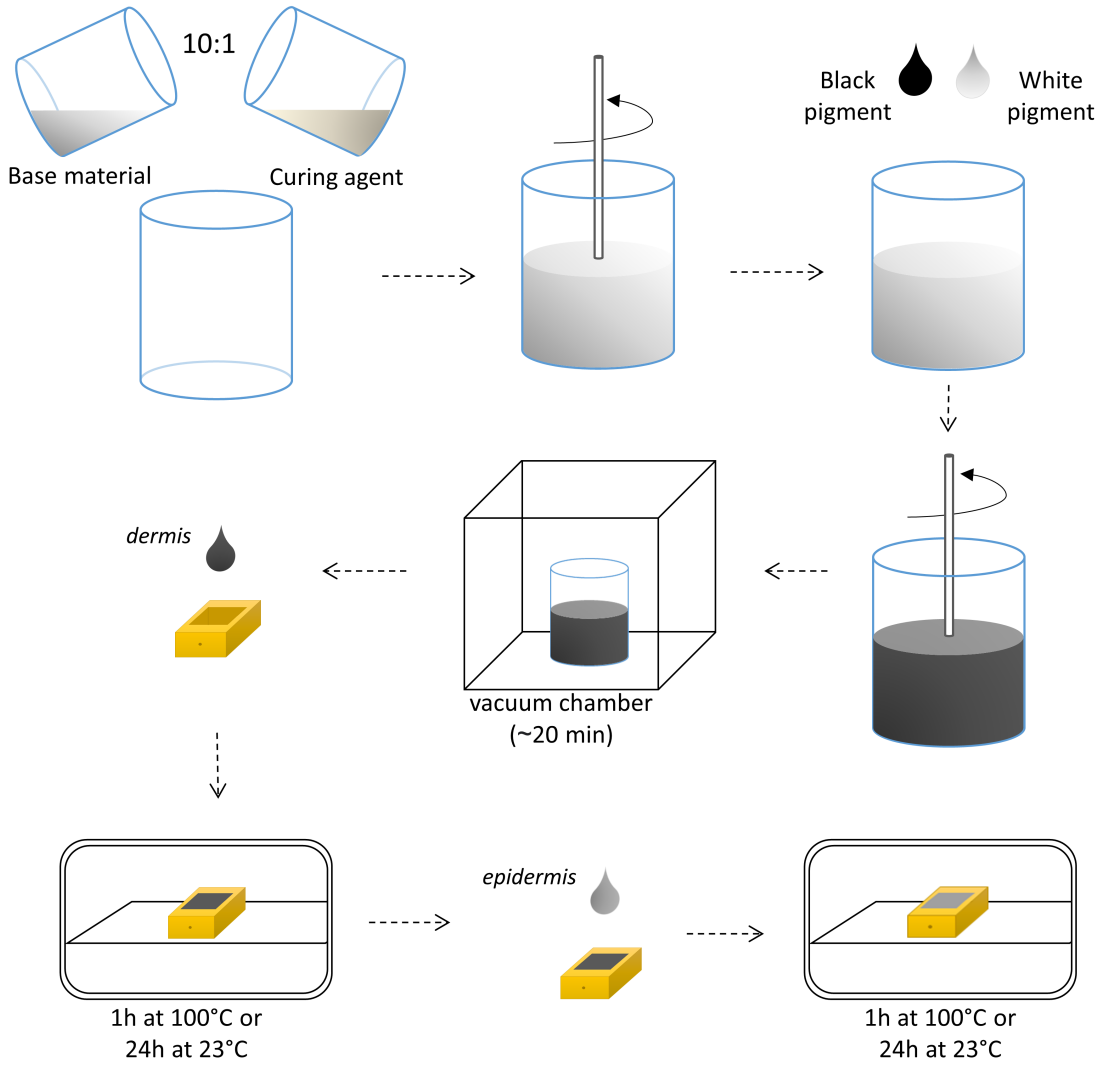

Figure 5.3: Summary of the steps for PDMS mixtures layering.

Tuning the weight percentages of black and white pigments it's possible to change

the optical properties of the material. Several combinations of the two concentrations bring to different values of the absorption coefficient and reduced scattering coefficient and so different behavior of the OCT signal as well. In order to obtain a realistic skin phantom, it's important to chose the optimal combination of concentrations able to yield an OCT signal comparable to the one from an in-vivo OCT acquisition in terms of intensity and penetration depth. In Tab. 5.1 are shown the values of nine combinations of weight percentages that were optically characterized previously to this work by the *OC-PAI* research group (MUW). In particular, the absorbance and reduced scattering coefficients were extracted measuring the diffuse reflectance and transmittance of light by the tissue samples using an integrating spheres system and then applying the inverse adding doubling (IAD) algorithm on raw data. The characterization results at 1300 nm are shown in Fig. 5.4: blue dots represent the nine combinations detailed in Tab 5.1 while red and pink dots represent the literature reference values [18] for dermis and epidermis, respectively.

PDMS	W01 (%w/w)	W02 (%w/w)	W03 (%w/w)
B01 (%w/w)	W: 0.36 % B: 0.18 %	W: 0.72 % B: 0.20 %	W: 1.31 % B: 0.16 %
B02 (%w/w)	W: 0.36 % B: 0.39 %	W: 0.70 % B: 0.40 %	W: 1.32 % B: 0.43 %
B03 (%w/w)	W: 0.35 % B: 0.63 %	W: 0.76 % B: 0.67 %	W: 1.63 % B: 0.65 %

Table 5.1 Nine combinations of black and white pigments percentages in PDMS for which the optical characterization at 1300 nm was available.

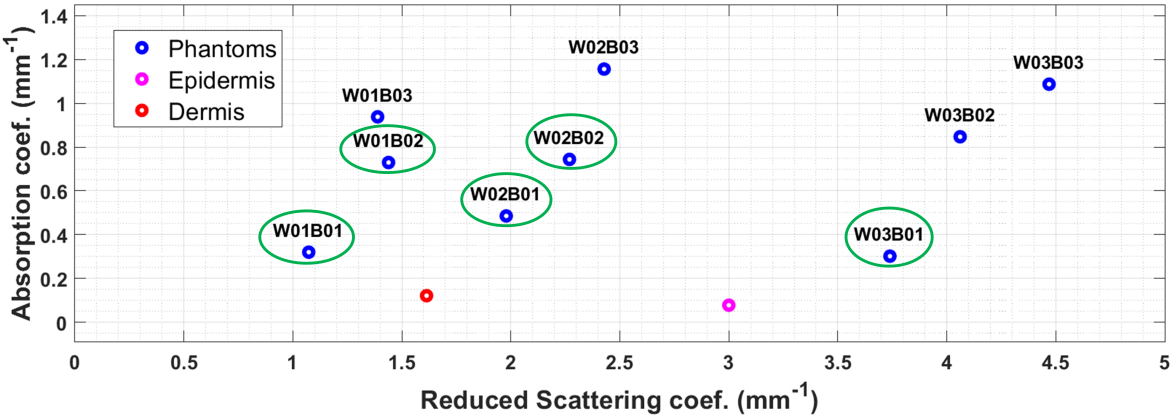

Figure 5.4: Optical characterization of the nine combinations of pigments collected in Tab. 5.1 (blue dots) and of literature reference values [18] (pink and red dots). Green circles highlight the combination used for further imaging characterization.

From Fig. 5.4, it can be seen that there's not a solution that perfectly matches both the scattering and absorption indexes literature values and more than one solution seems to be acceptable. Thus, in order to select two combinations for the two skin

layers, a characterization from an imaging point of view was needed as well to check if the penetration depths were suitable or not to show the vessel in the OCT images and eventually discard some options. The five combinations circled in green in Fig. 5.4 were then used for further tests with the OCT system. For each selected combination, a sample was prepared and poured into a Petri dish as describe before. The Petri dish was held slightly sloped during the curing phase (Fig. 5.5 A) so that, in the same dish, it was possible to check for different depth using the bottom of the Petri dish as a scatterer object to visualize (Fig. 5.5 B). As shwon in Fig. 5.5 C, after the curing process a slice of sample was cutted in the direction of the varying depths and removed. A caliber was used to identify and mark the location of the 1 mm depth and then the slice was reinserted into the Petri dish so that it was possible to acquire an OCT volume with the center B-scan approximately located on the 1 mm thickness of the PDMS mixture respect to the bottom of the dish and check for different depth around 1 mm.

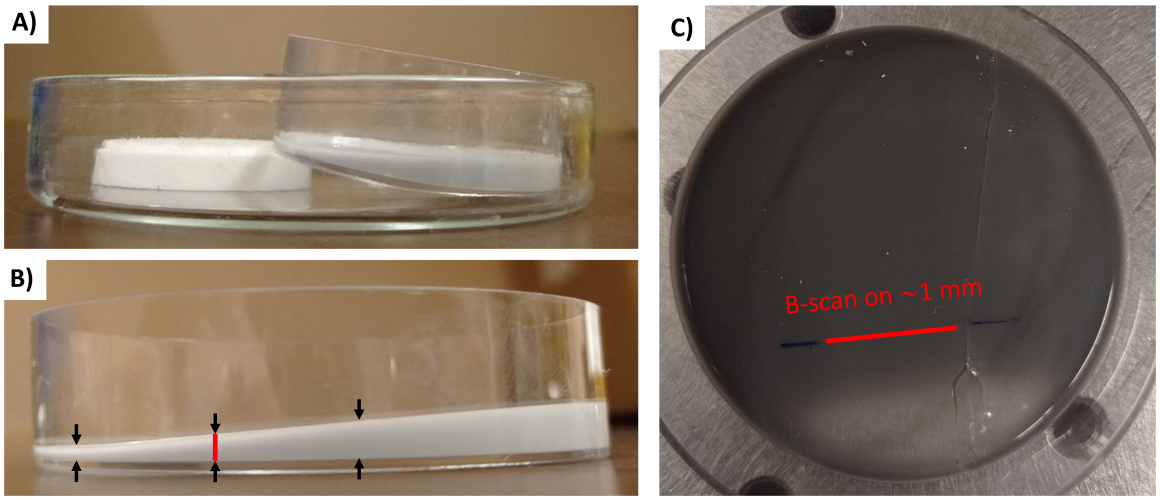

Figure 5.5: Preparation of PDMS mixtures samples with varying thickness. (A) Tilted position of the Petri dish during curing. (B) Different thicknesses of PDMS mixture obtained respect to the dish floor. (C) 1 mm thickness localization and marking for imaging field of view alignment.

During OCT volume reconstruction, the axial pixel size cannot be uniquely set since the exact refractive index for the five combinations of pigments in PDMS is not known. Thus, in a first moment the pure PDMS refractive index of 1.4 was used. The thickness of the Petri dish floor was measured to be 0.77 mm using a caliber. Then, comparing this value with the thickness resulting from the cross-section OCT image of the sample it was possible to individually rescale the vertical axis of each volume and locate the horizontal position where the PDMS thickness is about 1 mm. This position was highlighted with a red line in order to properly compare the results between different concentrations of pigments.

Evaluating both optical and imaging characterization results it's possible to select the best options for dermis and epidermis layers.

6. OCTA tests

6.1 Phantom assessment

During the phantom development, some tests were performed in order to check the successful outcome of each step.

After the 3D printing step, the resin structures were observed through an optical microscope in order to check for the integrity of the vessel and identify any imperfection due to printing itself or to a prolonged use of isopropanol. Then, two needles were fixed at the inlet/outlet holes so that isopropanol could flow inside the channel as well and remove uncured resin in the hollow internal part of the structure. Distilled water was then used to remove isopropanol. Also, simply adding red/blue ink into distilled water, it was possible to check if all the branches of the channel were open or not. If the dimension of the internal lumen was large enough, this first flow evaluation was simply made manually with syringes. Otherwise, an infusion/withdrawal syringe pump was used as it will described later.

Whether the outcome of these evaluations was satisfactory, the PDMS layers were added. The "dermis" layer was poured into the vat paying attention to leave enough space for a thin layer of "epidermis" and the epidermal thickness was then evaluated looking at the OCT B-scans.

6.1.1 OCTA acquisitions

The acquisition of OCT data on the phantom takes place into a set-up mainly composed of two parts: the OCT system itself and the perfusion path.

The OCT system was described in section 4. The steps related to the OCT system are: calibration and the consequent extraction of valid data points for data post processing; positioning of the phantom in a way that, along its path, the laser encounters only the phantom suspended in air; position and focus tuning of the laser thanks to the real-time preview of the acquisition system; quality signal optimization by adjusting the beam power, modifying the position of pedals for polarization matching and rotating the position of the probe respect to surface of the phantom to minimize artifacts due to the perpendicular reflection.

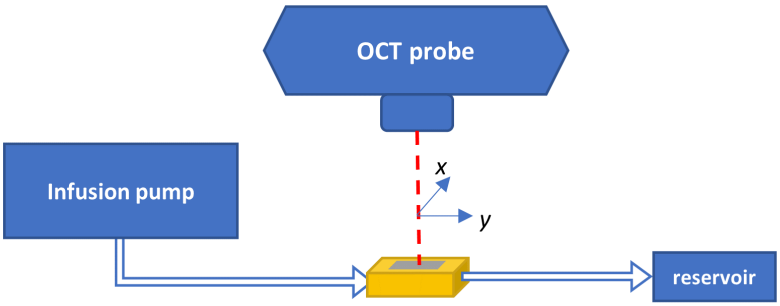

Figure 6.1: Acquisition set-up with perfusion.

As previously described, one important feature of a phantom produced according to the described approach is the possibility to perfuse it so that a realistic angiography can be acquired. For this purpose, the set-up for the experiment includes a microfluidic pump to let the desired fluid flow inside the phantom. The set-up is summarized in Fig. 6.1 and the details are reported below.

Microfluidic pump and perfused fluids

The pump implemented into the acquisition set-up is the *Pump 11 Pico Plus Elite* from *Harvard Apparatus*. It can accommodate syringes up to 10 ml and it's possible to set flow rates from 0.54 pl/min up to 11.70 ml/min. Several methods are available but the mainly used for this work was the "infuse only" method. Several syringes manufacturers and sizes can be selected to be used; however, the syringes used in these experiments was a 10 ml syringe from *Braun* with an inner diameter measured to be 15.9 mm and it was not listed; thus, a "custom syringe" was added. Knowing the desired flow velocity inside the phantom and the average area of its section, the corresponding flow rate could be calculated and set on the pump.

The perfused fluid should mimic the blood properties in terms of scattering/absorbing properties and size of the particles it contains. A mix of black ink and distilled water or whole milk and distilled water was used following the choices of some groups in literature [10].

The procedure for an OCTA acquisition was then composed of the following steps. Firstly, the syringe was filled with the fluid and connected to a tube paying attention to not include any air inside the circuit. The tube was then connected to one of the needles glued to the phantom, typically to the side from which the fluid could flow from smaller to bigger diameters reducing the chances to obstruct the channel. The pump was then turned on with a high flow rate, around 100 μl/min, until a couple of fluid drops were observed falling from the phantom outlet. In this way, the phantom was certainly filled with the new fluid even at the beginning of the acquisition. The desired flow rate was then selected on the pump and, after few minutes for flow settling, the OCT volumes could be acquired. After acquisitions, the vessels were accurately cleaned

with distilled water to avoid agglomeration.

6.1.2 OCTA reconstruction evaluations

In order to quantitatively evaluate the resulting angiographies, the overlapping percentage between the 3D model of the lumen used for printing and the OCTA volume segmentation was calculated for each phantom for which it was possible to totally assemble the layers, showing the potential of this phantom fabrication approach to test OCT systems as well as OCTA algorithms.

The *Matlab* array containing the OCTA data was imported in *Amira* to extract the segmentation. A generic segmentation pipeline was composed of: a 3D median filter for noise attenuation; a filter for z-drop correction to fix the signal attenuation due to the absorption in the upper layers; a filter for brightness and contrast improvement that adds an offset to each voxel and amplify the differences between each voxel value and the average value. Finally, a threshold was applied to discriminate voxels belonging to the vasculature and voxels belonging to the background. After that, some final cleaning operations were applied, such as removal of small objects and small islands so that only one connected object was segmented. The weights of each of this steps as well as the values for thresholding depend on the quality of the input OCTA volume.
After segmentation completion, the last step before comparing was the co-registration of the real and acquired volumes. For a valid and faster comparison, the volumes should be aligned and the bounding boxes of the volumes should have the same dimensions. Thus, an automatic *Amira* tool allowed to rotate and translate the volumes for alignment and then the cropping to the same dimensions was applied.

Once that both the objects were ready for comparison, they were exported as *Matlab* array so that the overlapping percentage could be easily performed. In particular, the Dice Similarity Coefficient was chosen for this purpose. It is defined as two times the intersection between the volumes divided by their union. It ranges from 0 to 1, where 0 means no overlap between the two sets and 1 means the sets are perfectly overlapped.

It is worth clarifying that the overlapping percentage it's not a consequence of the printing accuracy respect to the stl file of the vessel. The Dice value mainly depends on the OCT system penetration depth that could lead to signal loss from deeper vessels, on the strength of the projection artifact that causes over-segmentation and on the OCTA algorithm ability to selectively highlight the flowing fluid.

6.2 Wall thickness influence

As previously discussed, the resin wall thickness of the vessel introduces an extra interface that can lead to high contrast between the skin mimicking layers and the wall. However, in this approach the 3D printed vessel wall is the crucial element to obtain

very complex and realistic shapes of the channels. Thus, it's interesting to evaluate how this necessary element affects the signal and the estimation of the vessel lumen.

Whit this purpose, two phantoms with a straight channel characterized by the same diameter have been produced, one with the resin vessel wall and the other one without any wall between the PDMS and the lumen. The former was produced with the method described in the previous chapter using a straight channel of 140 μm in diameters as model of the vessel and adding a 20 μm thick vessel wall. The phantom without the wall was obtained printing the external vat without any vessel between the inlet and outlet holes so that later a copper wire (140 μm in diameter) could be inserted (Fig. 6.2a). To facilitate the copper wire inserting, a 400 μm drill bit was used to enlarge the inlet and outlet holes. Then, part of the same PDMS preparation used for the phantom with walls was poured inside the vat around the copper wire (Fig. 6.2b). Since the needle and the inlet/outlet hole are larger in diameter respect to the wire, some PDMS settles back inside the needle before the curing completion. However, if the wire goes through the needle as well, then the channel continuity is not compromised. After the curing process, the wire was gently removed leaving an empty straight channel.

Then, four OCT volumes were acquired on both phantoms using an experiment set-up for perfusion as described in section 6.1.1. The OCTA volumes were extracted using an intensity-based method ($iOCTA_{dec}$) and then the vessels were segmented and compared as described in section 6.1.2. Then, the overlapping between the volumes could be quantified. In order to compare each volume with the expected one, i.e. a straight channel with a circular section characterized by a 140 μm diameter, the average errors of the section areas in each B-scans respect to the expected one were calculated.

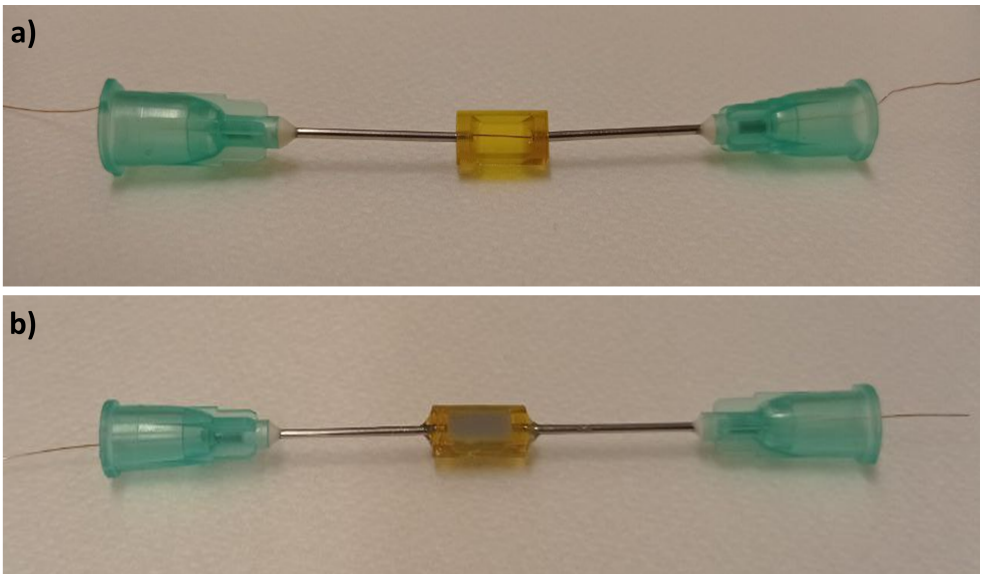

Figure 6.2: Development of a straight channel phantom without any vessel wall. (a) A copper wire is inserted into a 3D printed vat without any channel between the holes; (b) The PDMS is poured inside the vat using the wire as a mold for the vessel lumen.

6.3 OCTA vs flow velocity

As explained in section 2.3, the OCTA signal allows to extract the morphology of the vascular network but it contains the quantitative information about the flow velocity as well. The possibility to discriminate velocities based on the OCTA signal relies on both the interscan time and the flow velocity itself. If a BM-scan protocol is implemented, the interscan time depends on the B-scan size, thus on the field of view. It usually leads to interscan times of few milliseconds that bring the OCTA signal to saturate even for slow flow velocities. Nevertheless, even with the less sensitive interscan time, a difference between intensity from static and dynamic scatterers should be observed. The signal from steady fluids is typically higher than zero because of random noise, laser power oscillations and Brownian motion of the fluid itself. However, setting a proper threshold, the flowing fluid can be highlighted respect to steady one. In order to test the OCTA-flow velocity relation and find a proper threshold, some experiment were performed.

A first evaluation was the simple comparison between angiographies obtained on the phantom with no flow inside the channel and with the infusion pump set with a flow different from zero, using the standard protocol described in section 4.2 but fixing the B-scan position in order to observe the same pixels over time. In this first experiment, the implemented phantom was the so-called "Model 2 - Three branches model", described in section 8.1.2. The OCT signal acquired on the same fixed B-scan was composed of 1024 A-lines and then the interscan time was 4.5 ms. The number of B-scan repetition was 1024. Thus, for each pixel it was possible to extract 1021 OCTA signal values. The acquisition was performed with 0, 1, 5 and 200 μl/min as flow rates, corresponding to 0, 1.5, 7.4 and about 300 mm/s, respectively, considering the average diameter of 120 μm. Also, the values from a pixel belonging to the PDMS were taken into account as reference.
Similar experiments were also repeated simply reducing the FOV of each B-scan, i.e. the number of A-lines per B-scan, in order to reduce the interscan time.

To further characterize the system, the idea was to replicate, as much as possible, the experiment performed by Richter et al. [10] whose results are shown in Fig. 6.3. In that experiment, a MB-scan was implemented with 10 repetitions of the acquisition of the same A-line before switching to the next one so that the minimum interscan time could be exploited. Then, the 10 repetitions were simply downsampled to explore the complex OCTA for interscan times up to 90 μs.

Considering the tested OCT system, implementing a MB-scan protocol would have meant sending to the galvo mirrors a step function instead of a simple continuous increasing signal and it's not an ideal condition. Thus, the employed approach consist of reducing the FOV down to a single A-line aligned on the channel, fixing the B-scan position. In this way, even if a BM-scan protocol is implemented, the acquired volume is composed of the same A-scan at different moments and, for this specific system, each A-scan is acquired 4.5 μs after the previous one. Then, simply comparing 4 A-lines tem-

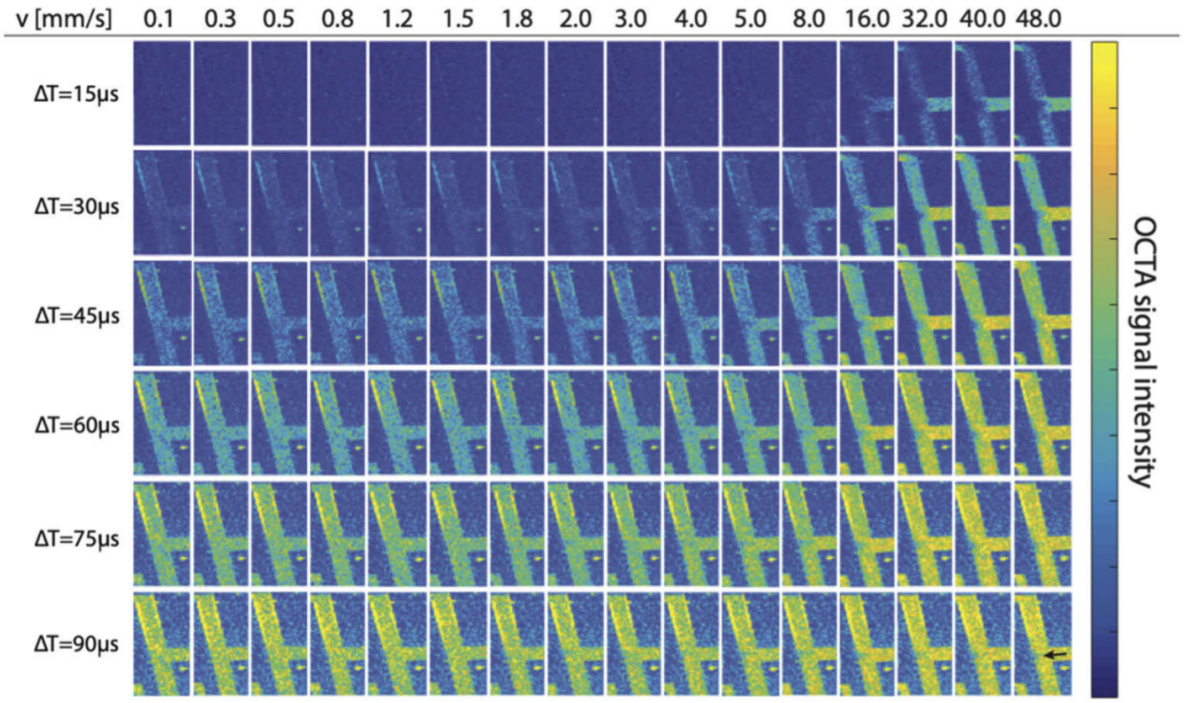

Figure 6.3: OCTA signal intensity for different interscan times ΔT measured at various flow rates. The arrow represents the flow direction. Adapted from [10].

porally spaced with a variable step, it's possible to explore different interscan times. Setting different flow rates on the infusion pump, flow velocities from 0 to 48 mm/s were explored, as well as in [10], plus a higher flow velocity of 80 mm/s. In order to replicate as far as possible the results, a mix of whole milk and distilled water with a ratio of 1:10 was used.
Firstly, the test was performed on a simple tube with an inner diameter of about 800 μm gluing the needle of the syringe inserted into the infusion pump to the tube itself. The bigger and known dimension helped with the alignment of the acquired A-line. For this experiment, the acquired volumes were composed of 512 B-scans and 1024 A-scans per B-scan. Even if the laser position should be fixed, in order to avoid eventual errors due to the unknown galvo flyback time, the OCTA values were extracted comparing only OCT A-lines belonging to the same B-scan. Each B-scan content was downsampled according to the interscan time of interest and, starting from the first A-line of each B-scan, one cOCTA A-line was extracted from each B-scan, obtaining 512 cOCTA A-lines. Thus, considering 4 OCT A-lines to compare, the maximum interscan time that could be investigated was $4.5\ \mu s * (1024/(4-1)) = 1.5$ ms. This method is summarized in Fig. 6.4.
Then the test was repeated on one of the phantoms developed during this work so that it was possible to characterize the system in a realistic condition as well. The phantom used for this experiment is the "Model 2 - Three branches model" and will be described in section 8.1.2. The inner diameter changes along the channel but considering the range of inner diameters between the inlet and the branching point, an average diame-

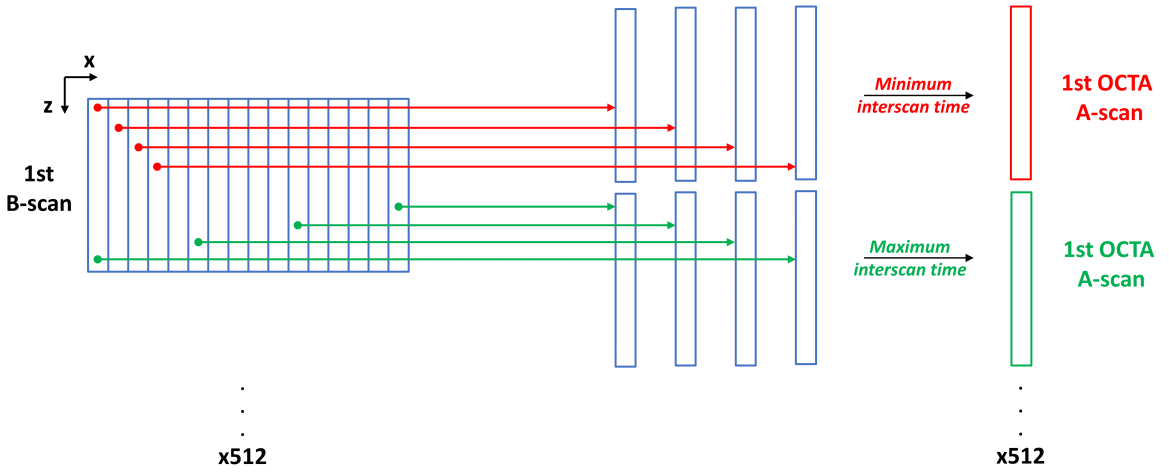

Figure 6.4: Summary of the method used to extract OCTA with different interscan times. All the A-scan are acquired in the same position. Within the same B-scan, groups of four A-scans are taken with different spacing to obtain one OCTA A-scan. The process is repeated for each B-scan.

ter of 120 μm was used to set the right flow rates in order to obtain the same previous velocities. In this case, an additional acquisition was taken aligning the laser out of the channel so that reference values from the steady PDMS could be extracted. For this experiment, the acquired volumes were composed of 32 B-scans and 32768 A-scans per B-scan. Then, always comparing OCT A-lines belonging to the same B-scan, it was possible to investigate higher interscan times, up to 4.5 ms. In this experiment, because of the critical issues when phase information is exploited, the intensity-based logarithmic OCTA was used and both Gaussian windowing of the raw data and Wiener filtering of the OCT volumes were applied.
Different steps of downsampling were taken into account. Then, for each velocity and for each interscan time, about 1000 angiographies (depending on the B-scans size) were extracted from groups of four OCT A-lines so that the average OCTA A-line characterizing each combination could be shown and the average OCTA value for a voxel belonging to the lumen could be plotted as a function of flow velocity. Also, a box-plot representation was used to show the variability of each case and evaluate the possibility to set a threshold.
In this case, since the B-scan size was bigger, higher interscan times could be investigated. Thus also the value of 4.5 μs used in the standard protocol was explored.

Part III

Results and discussion

7. Preliminary tests

7.1 Pigments concentration

As previously described, the available optical characterization for nine combinations of white and black pigments percentages in weight respect to the PDMS doesn't highlight a combination that perfectly matches the reference values for dermis or epidermis. Thus, for each of the five combinations selected in Fig. 5.4, a sample was prepared and imaged as described in section 5.3. In Fig. 7.1 are shown the OCT cross-sections for each sample and the red lines highlight the position corresponding to a PDMS thickness of about 1 mm. As expected, higher concentrations of pigments lead to a signal quality decrease since the amount of light absorbed or scattered per unit of length is higher.

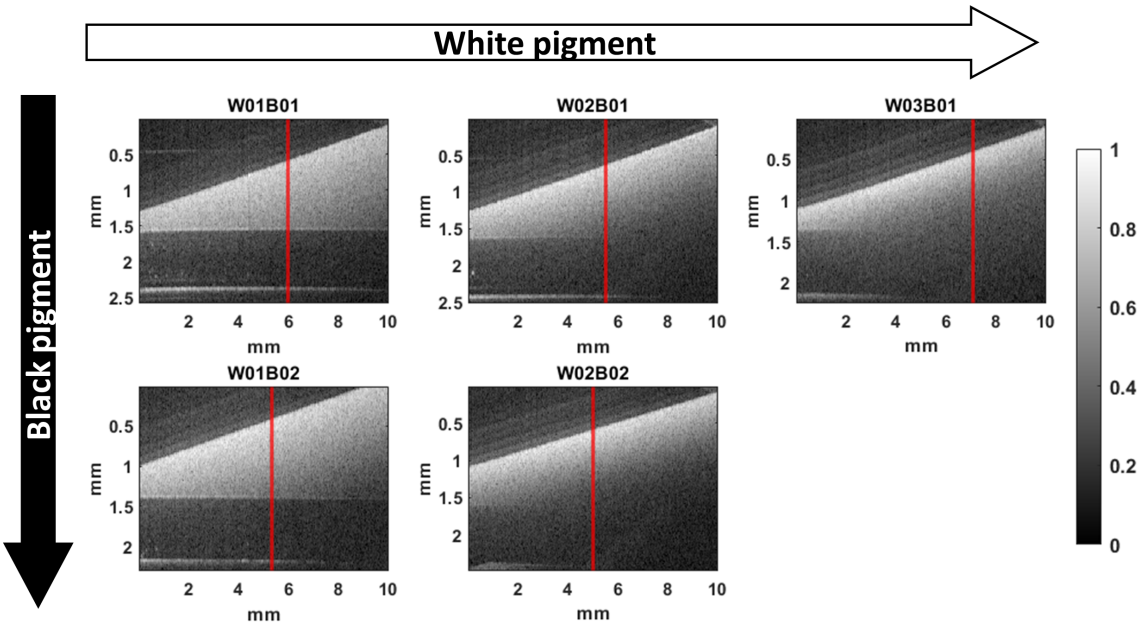

Figure 7.1: Imaging assessment for the five selected combinations of additive percentages in PDMS over different depths. The red lines are located on the thickness of about 1 mm.

The dermis-mimicking layer will be the thickest one and will fill the whole vat except for few hundreds of μm on the upper surface where the epidermis-mimicking layer

will be cured. Then, considering the phantoms developed during this work, since the deepest vessel was located at about 1.7 mm from the surface, the best option to mimic the dermis layer turned out to be the so-called "W01B01" that showed a clear signal from the Petri dish floor even where the PDMS thickness is the higher between the explored depths, about 1.5 mm. Also, referring to the graph in Fig. 5.4, the "W01B01" combination is, at the same time, close to the dermis reference values but also far enough from the epidermis ones.
Similarly, both the "W02B01" and the "W03B01" could potentially properly mimic the empidermis layer. Considering that this layer should be about 100 μm in thickness, looking at the left end of the relative graphs, the effects of both these combinations seem to be similar. However, since the layers thickness is not accurately adjustable and repeatable, the "W02B01" was chosen in order to limit the effect on the signal in case of thicker epidermis layers.
The resulting optical properties in terms of reduced scattering coefficient and absorption coefficient are 1.07 $mm^{-}1$ and 0.32 $mm^{-}1$ for dermis and 1.98 $mm^{-}1$ and 0.48 $mm^{-}1$ for epidermis, respectively.

In the next chapter are shown the OCT and OCTA results with both the layers for the developed phantoms.

7.2 Resin vessel wall

The resin vessel wall effect was evaluated from an OCT/OCTA signal intensity point of view and also the effects of the lumen diameters were taken into account.

As described in section 6.2, the vat used for the wall-free phantom was about 6 mm in length instead of the 3.5 mm usually characterizing the vat length. Thus, the acquired volume was cropped so that the observed channel was as long as the one with the wall, centering the cropping window on the center of the channel itself. An OCT B-scan acquired with a flow rate of 10 μl/min for both the phantoms is shown in Fig. 7.2 A and B. Then, Fig. 7.2 C shows the plot of an A-line centered on the channel from both the B-scans. The two A-lines were aligned respect to the fist peak corresponding to the air-PDMS interface. The graph shows that the OCT signal intensity decrease is equivalent. However, because of the holes enlargement with the micro drill bit, the copper wire position during the curing phase wasn't exactly the same of the lumen in the phantom with the vessel wall. Aligning then the two A-scan respect to the position of the lumen, it's possible to observe the difference behavior of the OCT signal around the channel location. In particular, the signal peaks from the resin vessel walls results to be higher and wider respect to the ones from the PDMS-lumen interface. The peaks originates because, considering the rounded shape of the wall or the interface, there will be a location in which the light hits that interfaces in a perpendicular way. Then, the reflected light in that direction, i.e. the OCT signal, is higher.

The angiography segmentations were then compared. The Matlab arrays containing

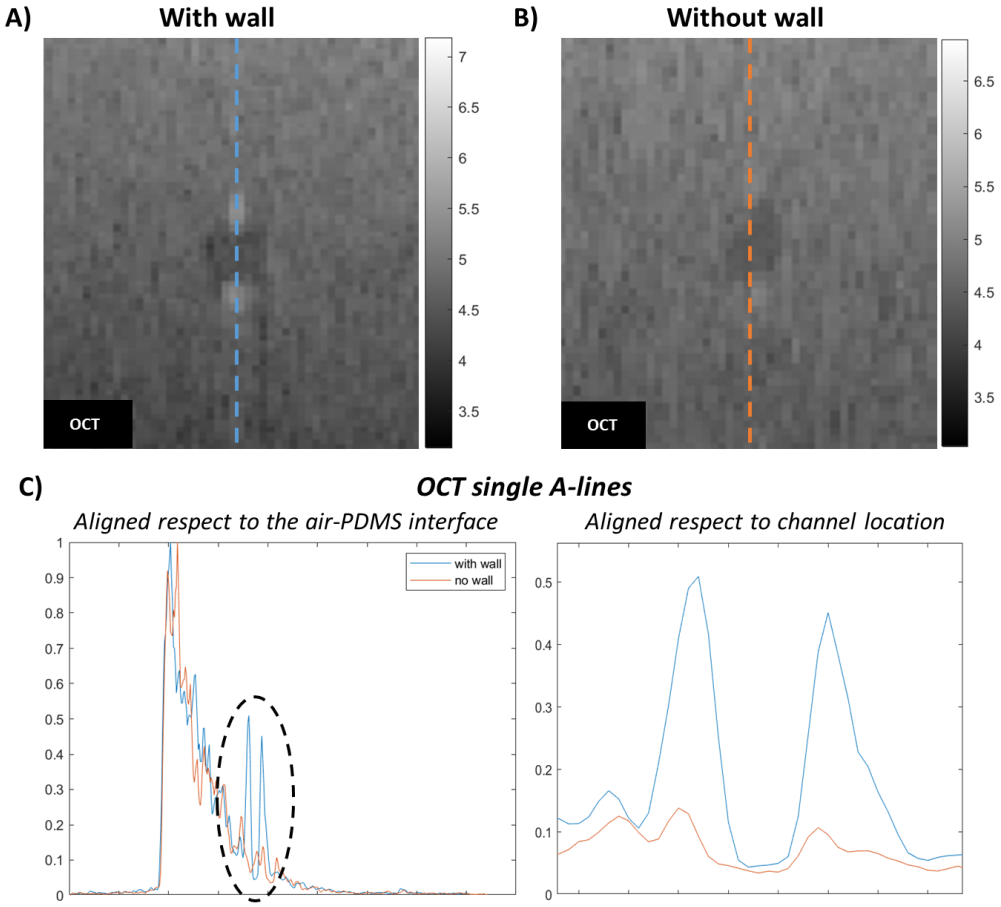

Figure 7.2: Resin vessel wall effect on OCT signal. (A) OCT B-scan of the phantom with the 3D-printed channel. (B) OCT B-scan of the phantom with the channel without any vessel wall. (C) Plot of the A-lines highlighted in blue and orange in (A) and (B), aligning them respect to the air-PDMS interface and to the channel location.

the co-registered vessel intensity-based angiographies were processed and segmented as described in section 6.2 obtaining the lumen diameters map showed in Fig. 7.3. The two volumes are characterized by a Dice similarity coefficient of 73%. Then, the average error of the lumen area in the B-scans respect to expected area of a circle characterized by a diameter of 140 μm were calculated to be +8.6% and +7.7% for the channel with the vessel wall and the one without any wall, respectively. In both cases, the over-segmentation is mainly due to the projection artifact that causes the segmented area to be stretched downwards.

Thus, in view of these results, it can be stated that the resin vessel wall doesn't introduce a significant effect on the OCTA signals as well as on the angiography segmentation, probably as a consequence of the projection artifact extent that makes any variations due to the wall presence negligible.

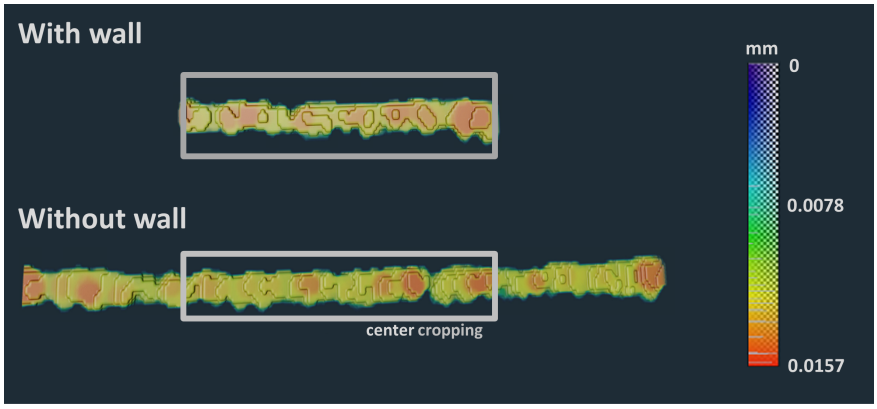

Figure 7.3: Diameter maps of the segmented results. The gray squares contain the volumes that were compared through the Dice coefficient.

7.3 OCTA signal vs flow velocity

The first experiment to characterize the OCTA signal - flow velocity relation was performed on the so-called "Model 2 - Three branches model" fixing the B-scan position and investigating four velocities, using both undiluted whole milk and black ink. To identify the pixels belonging to the lumen, the standard deviation between the 1024 acquired B-scans was performed. Then one pixel inside the lumen was selected (red squares in Fig. 7.4) and its intensity-based logarithmic OCTA values were collected in the form of a box-plot for each velocity. These results for whole milk and black ink are shown in Fig. 7.4. For the experiment with black ink as perfused fluid, the 200 μl/min flow rate is not available.
From the results, it can be observed that, taking the average value from the pixel belonging to the PDMS as reference for the steady scatterers, all the explored velocities result to have an average OCTA value higher respect to the PDMS pixel but it's not possible to set a threshold to discriminate slow and fast velocities. Indeed, the OCTA average values inside the lumen are comparable and don't show any trend. Also, the signal ranges covered by the box-plots are wide due to a variability of the OCTA signal that occurs even keeping constant the experimental variables, such as the flow rate and the A-line location. Furthermore, even from the acquisition preview, it could be clearly seen that the OCT value of the pixel inside the lumen changes more respect to the surrounding ones when no flow rate is applied. In Fig. 7.5 are shown some frames relative to 0 μl/min after Matlab OCT signal extraction where inside the red circles it's possible to notice the lumen pixel changes, while in blue circles it's clear that OCT signal from PDMS is more stable. Thus, it's clear that the reason why an OCTA signal originates from the fluid even when no flow is set on the pump is that, anyhow, the fluid is moving. The main hypothesis to explain this behavior is that the laser itself, hitting the fluid in order to probing it, heats locally the fluid putting it in motion. Also, the system's sensitivity to Brownian motion it's not known.
The same experiment was repeated after emptying the vessel so that the signal from air inside the channel could be extracted and used as reference for discussion. In Fig.

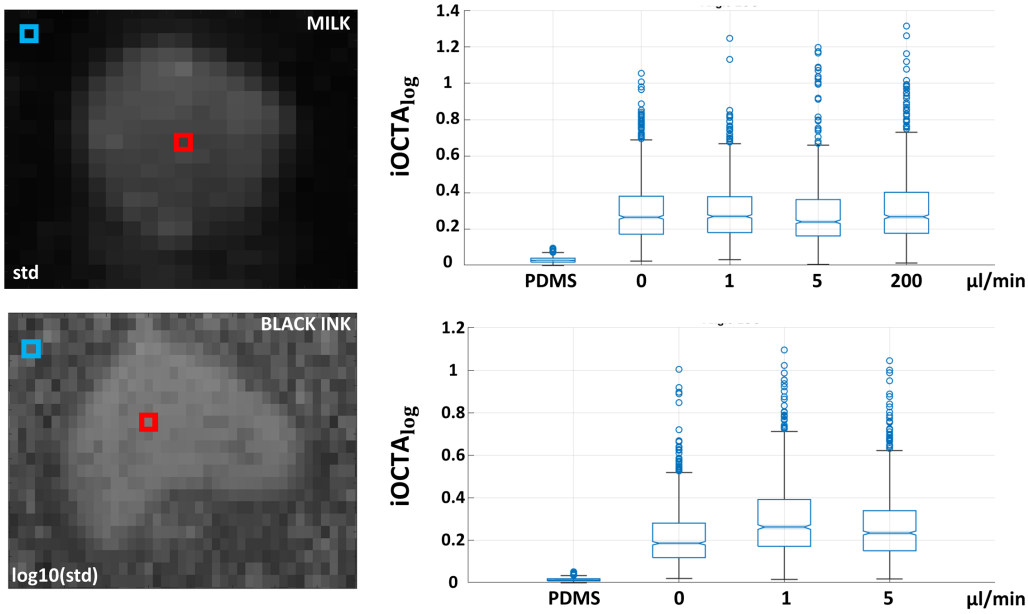

Figure 7.4: Results of the OCTA signal extraction over time for the same pixel belonging to the lumen (red square) for different velocities and for a pixel belonging to the PDMS (blue square). Each set of OCTA values over time is collected into a bloxplot. The first and second rows show the results using diluted milk and black ink, respectively.

7.6 is shown the result compared to a pixel belonging to the steady PDMS.

A second experiment was then performed reducing the B-scan size to 50 A-lines, enough to still observe the whole vessel section but with a lower interscan time, around 0.22 ms. In this case the investigated velocities range was extended to twelve values from 0 to about 150 mm/s. Also, because of the hypothesis of the motion caused by the laser heating, the 0 mm/s test was repeated turning off the laser during the fluid settling time and turning it on just before the acquisition.
The iOCTA box-plots of a pixel inside the lumen were extracted: turning the laser off before the acquisition doesn't have a significant effect on the results. Thus, it's likely that the acquisition time is enough for the laser to heat the fluid and put it in motion. Also, the average OCTA values and the width of the box-plots of each velocities are still so overlapped that not any threshold could be set to discriminate slow and fast velocities. About that, it must be taken into account that obtaining the interscan time as the number of A-lines per B-scan by the inverse of the A-scan rate is an approximation because it doesn't consider the galvo flyback time that is needed to pass from the last A-line of a B-scan to the first A-line of the consecutive one. Since the flyback time is unknown, it's appropriate to specify that the interscan time of 0.22 ms is underestimated.

In order to investigate as much as possible the relationship between OCTA signal and

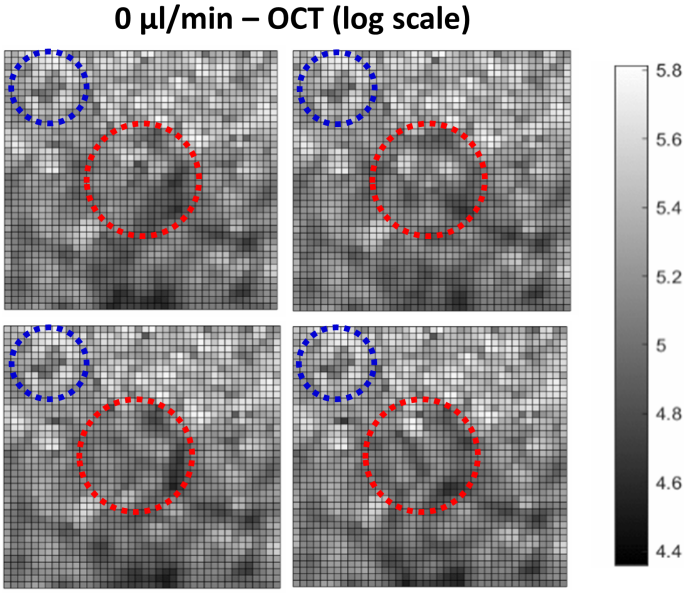

Figure 7.5: Four different frames over time showing the OCT B-scan when a 0 μm flow was set. The red circle highlight the changes inside the lumen. The blue circle highlight a PDMS region.

velocity over different interscan times, the experiment shown in Fig. 6.3 was reproduced as faithfully as possible, as described in section 6.3. Thus, with regard to the experiment performed on the 800 μm tube, the grid showing the average OMAG A-line for each combination of interscan time and velocity with a common color-map is shown in Fig. 7.7. Also, in order to assess for the minimum velocity that leads to the saturation level, it's useful to represent the same information through a graph specifically for one pixel belonging to the lumen (Fig. 7.8).

The results are consistent with the reference ones and it can be stated that, from an average point of view, the velocity at which the saturation level is reached decreases as the interscan time becomes longer. Also, when no flow rate is set, not only the OMAG signal is higher than zero but also it increases as the interscan time increases, confirming that in that situation the fluid is moving.

With the purpose to set a proper threshold in the signal processing pipeline to isolate the flowing fluid, not only the average trends should be observed but also the variability of the signal for each combination of velocity and interscan time. The eight graphs in Fig. 7.8 are now detailed in Fig. 7.9 with the box-plots of the set of OMAG values obtained for each combination.

Again, the OCTA signal variability turned out to be so wide to cover any differences in mean values for different velocities that occur for lower interscan times. At his point, the main hypothesis to explain this behavior is that such signal variability could be due to an electronic noise from the data acquisition system. Anyway, for the purpose of this thesis, demonstrating that the reason why it's not possible to discriminate slow flow velocities from fast flow velocities is due to the long interscan time, is enough to validate

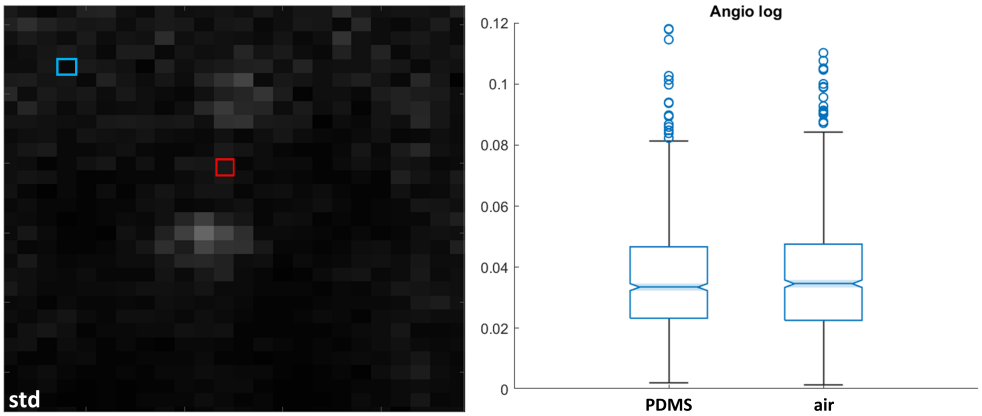

Figure 7.6: Boxplots of the OCTA signal over time for a pixel belonging to the lumen (red square) and a pixel belonging to the PDMS (blue square).

the angiography results. Also, considering the physiological blood flow velocities of 0.4 - 0.9 mm/s, it's clear that even with the shortest interscan time possible for this OCT system, all the blood will be highlighted in the same way, either moving or not. However, the skin tissue layers, i.e. the PDMS, don't generate any significant OCTA signal as stated from the previous experiments, allowing to obtain a proper angiography. Similar results were obtained with an intensity-based OCTA algorithm.

In order to obtain a realistic characterization of the OCTA signal - interscan time relation, the same experiment should be repeated on a phantom, so that a realistic set up could be mimicked. The tested phantom was again the so-called "Model 2 - Three branches model". As discussed in section 6.3, in this case an iOCTA algorithm (4.3) was applied instead of the OMAG one because of the critical issues when phase information is exploited. Similarly to the previous experiment, in Fig. 7.10 and 7.11 are shown the average results and in Fig. 7.12 the details about signal variability. In this case, the acquisition allowed to explore longer interscan times. Thus, two additional interscan time of 2.25 ms and 4.5 ms were investigated.

As expected, the results show a behavior similar to the one obtained with OMAG signal from the tube. In this case, obtaining a successful experiment required more effort because of the smaller inner diameter that made the laser alignment more difficult. Also, considering the time needed to settle each flow, the acquisition time and the data saving time, it could happen that during the experiment a phantom movement occurs. Then, the relative position of the phantom respect to the laser could change between acquisitions at different velocities. This issue didn't affect the result obtained on the tube because of the bigger diameter and the constant shape of the tube so that even if a movement occurs the laser is still aligned. On the phantom, considering the diameter around 100 μm and the complex morphology, even the smaller displacement can invalidate that acquisition. Indeed, in Fig. 7.12, considering the highest interscan time that should give always a signal at a saturation level, it can be seen that the extent of

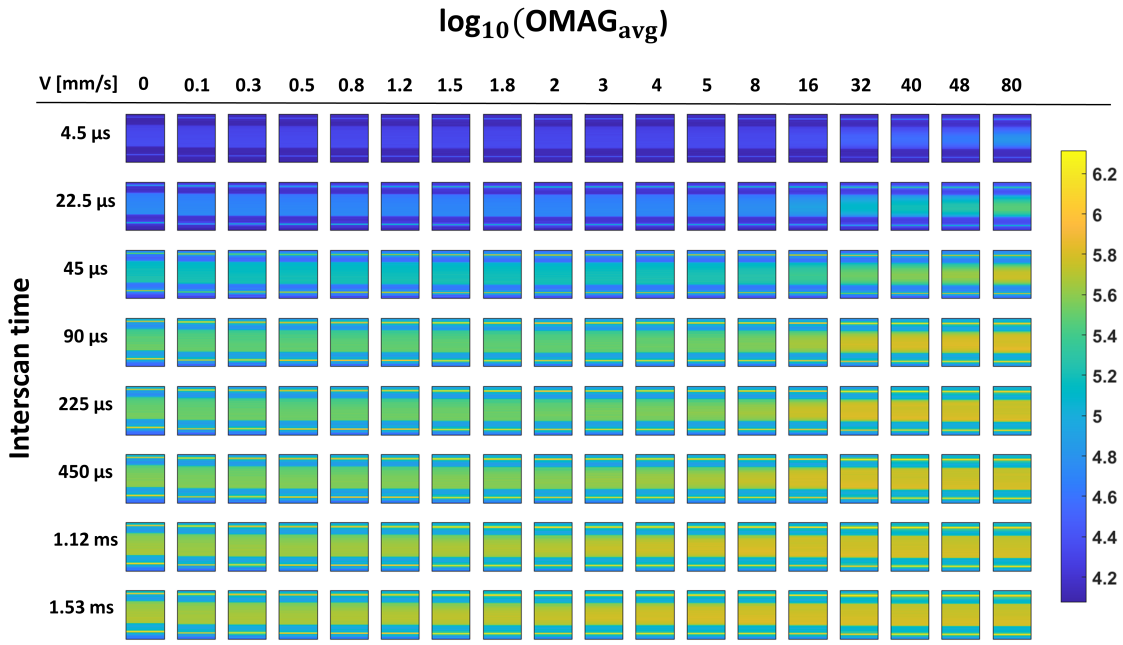

Figure 7.7: OCTA signal testing on the tube: average OMAG magnitude for one A-line centered on the 800 μm tube for different flow velocities and interscan times.

the imaged lumen and the location of its center seem to change between each velocity acquisition. The initial alignment was made trying to hit the center of the channel so that the simply considering the pixel in the middle of the lumen it could be possible to exploit the maximum velocity according to the velocity profile of a fluid in a channel. Thus, the consequence of a displacement could be that, even if the laser always hits the lumen, an additional error could affect the real flow velocity. Also, it's not clear why the 48 mm/s acquisition shows a striped pattern. It could be due to a noisy acquisition or maybe to some micro bubble in the fluid.

Summing up the results, it was verified that the combination of the employed OCT system and OCTA algorithm can properly distinguish dynamic and static scatters but, with the currently used set up and acquisition protocol, it's impossible to set a threshold to distinguish flowing and steady fluid because the resulting OCTA signals are comparable. A possible explanation could be a very high sensibility of the system to Brownian motion or rather that there are some factors that induce motion even when not any flow rate is set on the pump, such as local heating by the laser beam during acquisition or gravity that let particles moving inside the lumen if it's not perfectly horizontal. Considering the focus of this work, as long as there is a clear difference between signal from the blood-mimicking fluid and the PDMS layers, the results can be considered reliable. Actually, this "issue" helps during phantom OCTA evaluation: if not any OCTA signal is observed from deeper branches, then it's certainly due to the limited penetration depth of the OCT system and not to the vessels design that

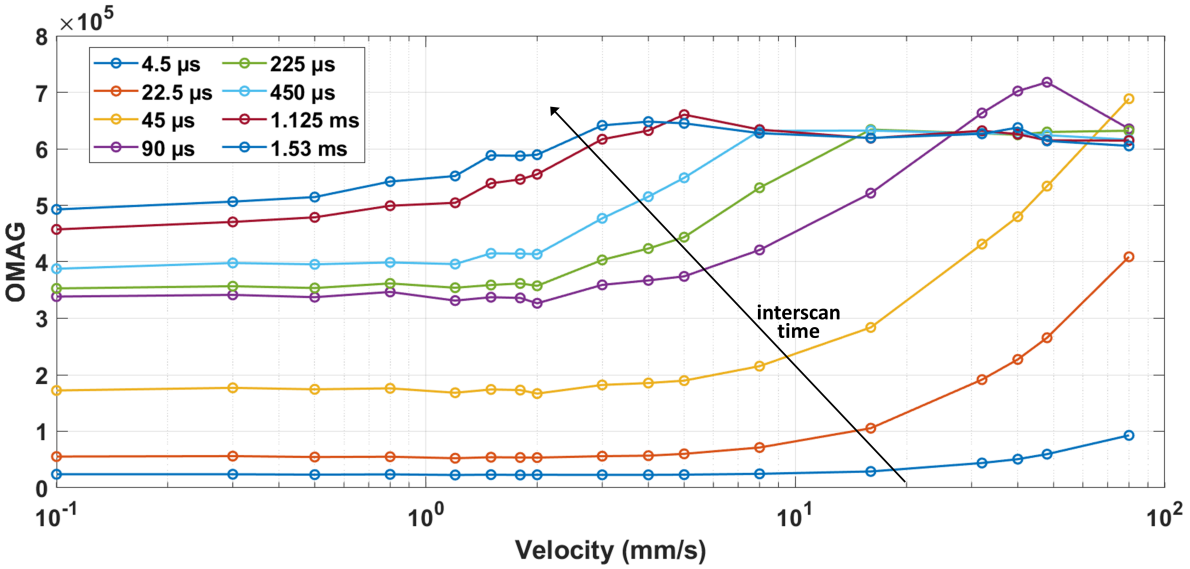

Figure 7.8: Plot of the average OMAG magnitude over flow velocities for one pixel belonging to the tube lumen for different flow velocities and interscan times.

eventually causes slower flow velocities in some branches. Even if this situation occurs and the fluid is steady in some branches, OCTA signal would be observed anyway. Another result is the variability of each observation. Considering for example the interscan time of 90 μs for the tube experiment in Fig. 7.7, the average behavior of OCTA signal over flow velocity would allow to set a threshold to highlight only fast velocities but the signals variability is so wide that the ranges of each observation totally overlap. A possible explanation could be some source of noise from the components of the acquisition system that cannot be removed via software. The possibility of an additional variability introduced by the oscillatory mechanism of the infusion pump was investigated but not any oscillatory pattern was found in the signals over time. It would worth to further investigate this possibility with acquisitions over a longer time. However, also in this case the results can be considered reliable since the difference between dynamic and static scatters can be properly observed.

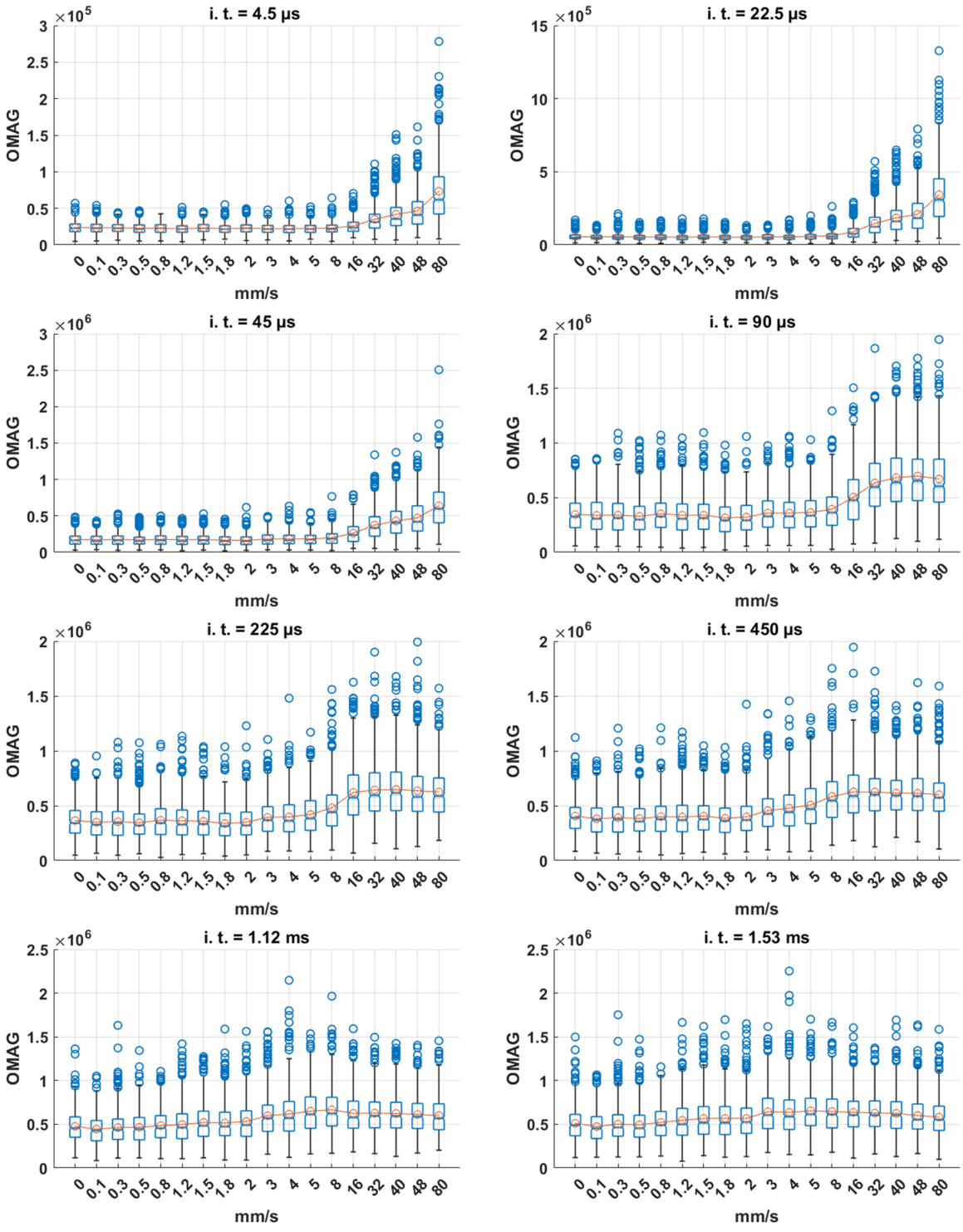

Figure 7.9: OCTA signal testing on the tube: boxplot representations of the signals shown in Fig. 7.8.

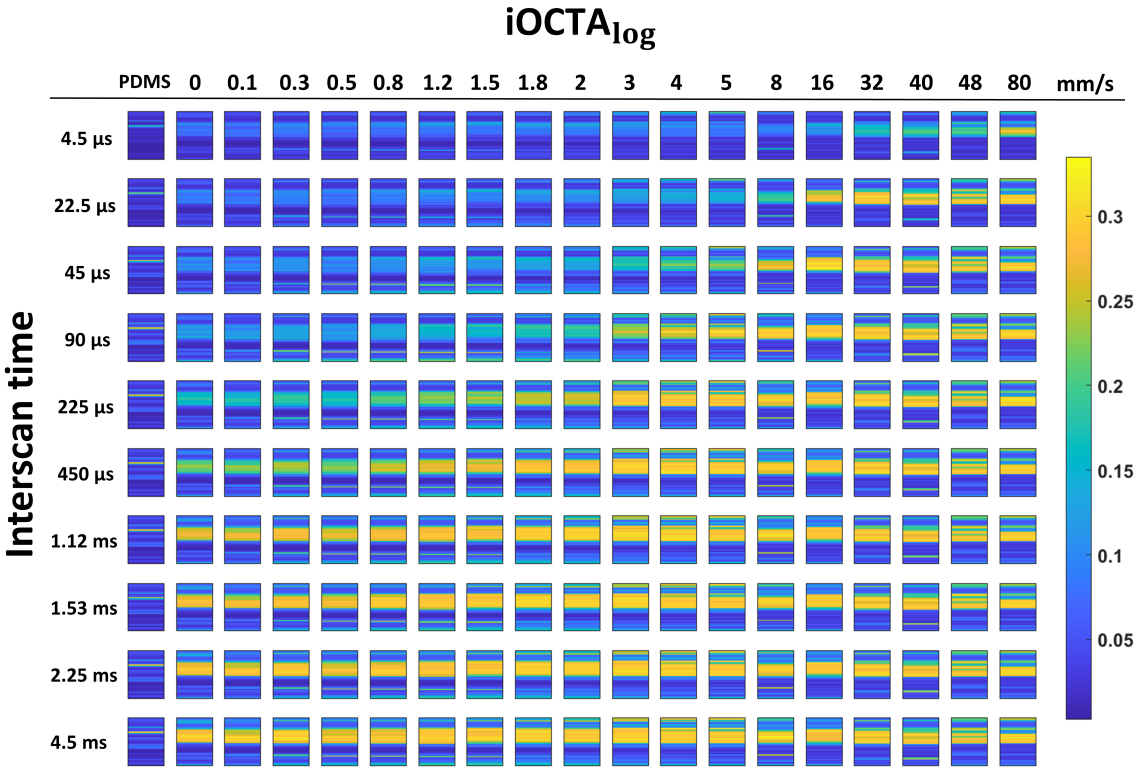

Figure 7.10: OCTA signal testing on the phantom: average logarithmic intensity-based OCTA for one A-line centered on the vessel for different flow velocities and interscan times.

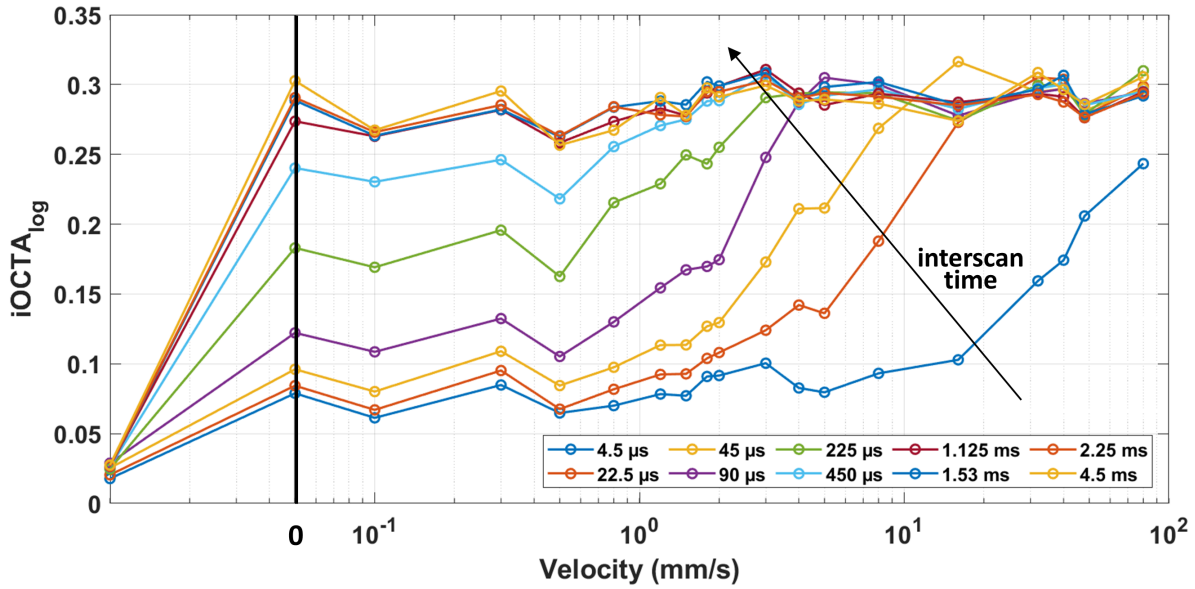

Figure 7.11: Plot of the average logarithmic intensity-based OCTA over flow velocities for one pixel belonging to the vessel lumen for different flow velocities and interscan times.

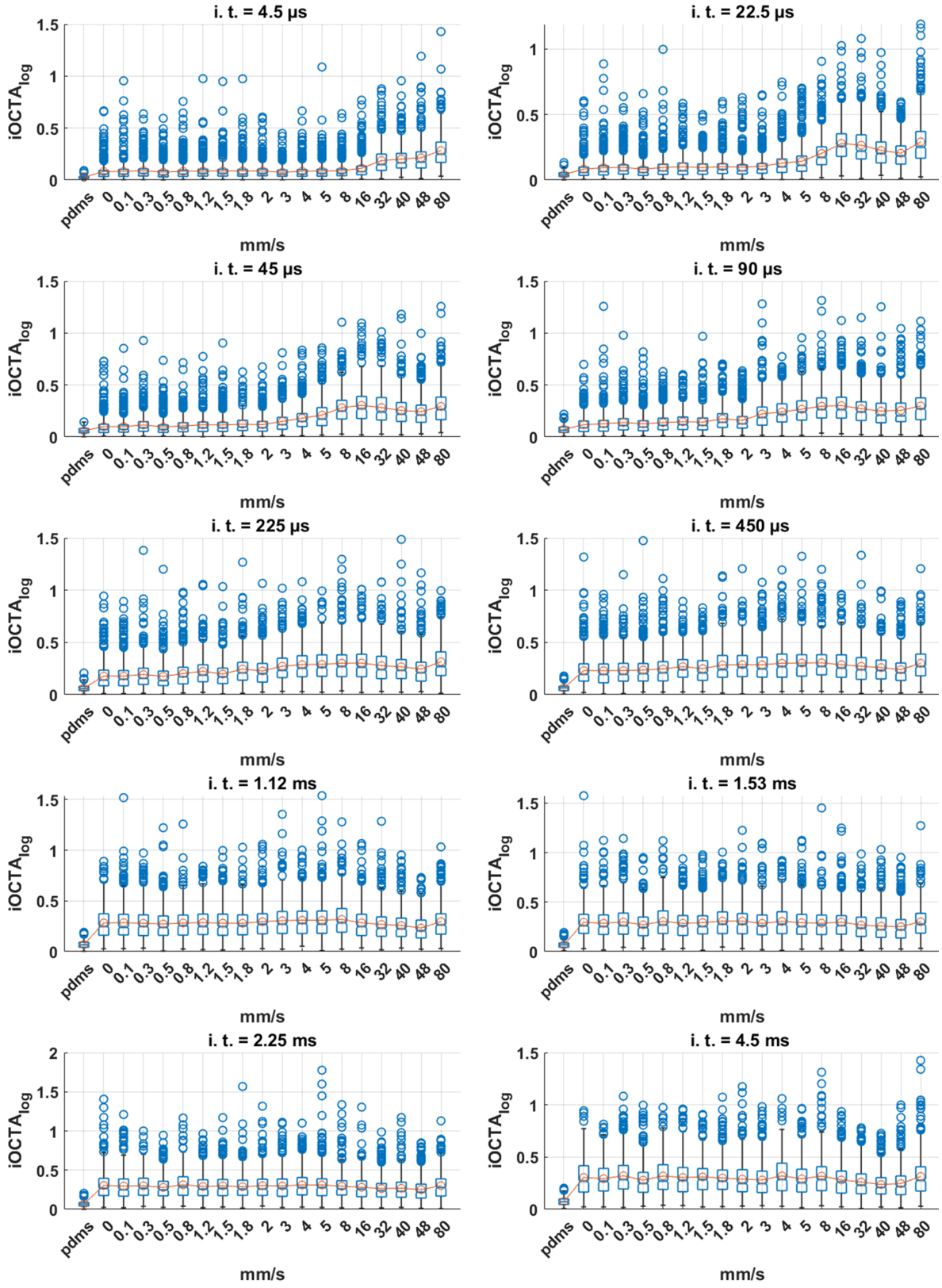

Figure 7.12: OCTA signal testing on the phantom: boxplot representations of the signals shown in Fig. 7.11.

8. Microvasculature phantoms

8.1 Healthy models

8.1.1 Model 1 - Five branches model

The first printed model comes from the segmentation of the thumb arterioles network shown in Fig. 5.1(a). One vessel was selected to be the internal lumen model of this phantom because of its simplicity and the continuity of its shapes that make it easier to be printed. The vessel was further processed as described in section 5.1, cutting the data from a certain depth in order to remove smaller capillaries. In Fig. 8.1 are shown the 3D volume processing steps performed with *Amira*, starting from the selected vessel up to the complete model of the clean vasculature inserted inside the vat.

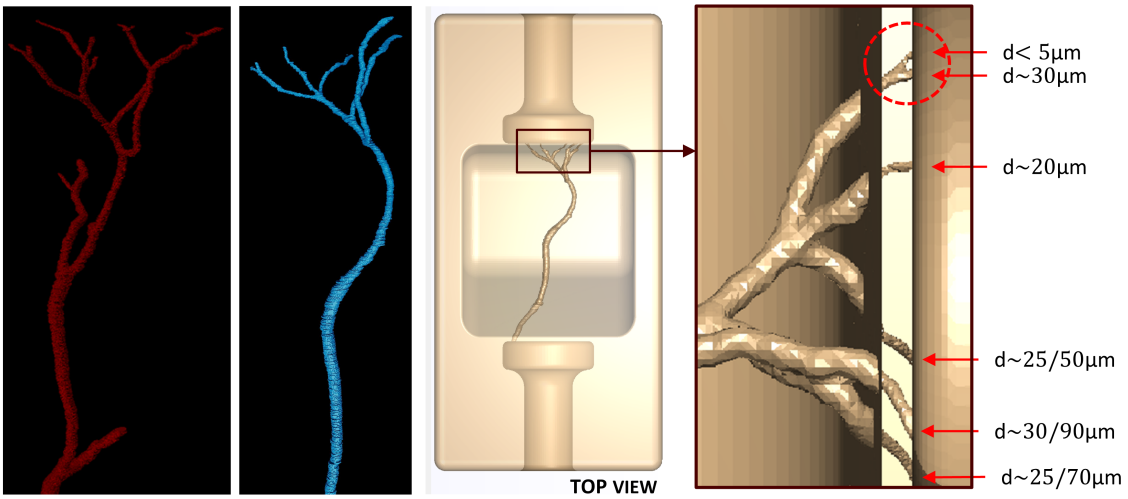

Figure 8.1: 3D processing steps from the selected vessel to the final complete stl file. In the last image are shown the final diameters or the two values of the major axes for the five branches. The red circle shows an error in the model.

The model is composed of a main channel that branches out into five paths. The diameter of the internal lumen decreases from 100 μm in the main channel up to 20 μm in the the final sections of the branches. The values of the five final sections area are shown in the last image of Fig. 8.1. Because of an error in the 3D model, the upper

branch has a bifurcation inside the resin of the vat: the parts inside the resin are not of interest for the purpose of this work and in this case the risk is to have a close path because of the final section diameter below 5 μm. Thus, more attention was paid for next models.
As discussed in chapter 5.1, the wall thickness should be kept as thin as possible, depending on the complexity of the structure. A value of 20 μm turned out to be thick enough to prevent the structure from collapsing under its own weight, even if the total length of the vessel had to be kept to 3.5 mm.
The position of the vessel respect to the external mold was chosen in a way that, in the top view, the five branches overlapped as little as possible and could be easily observed.

Preliminary evaluations

In Fig. 8.2A is shown the printed model through the optical microscope.

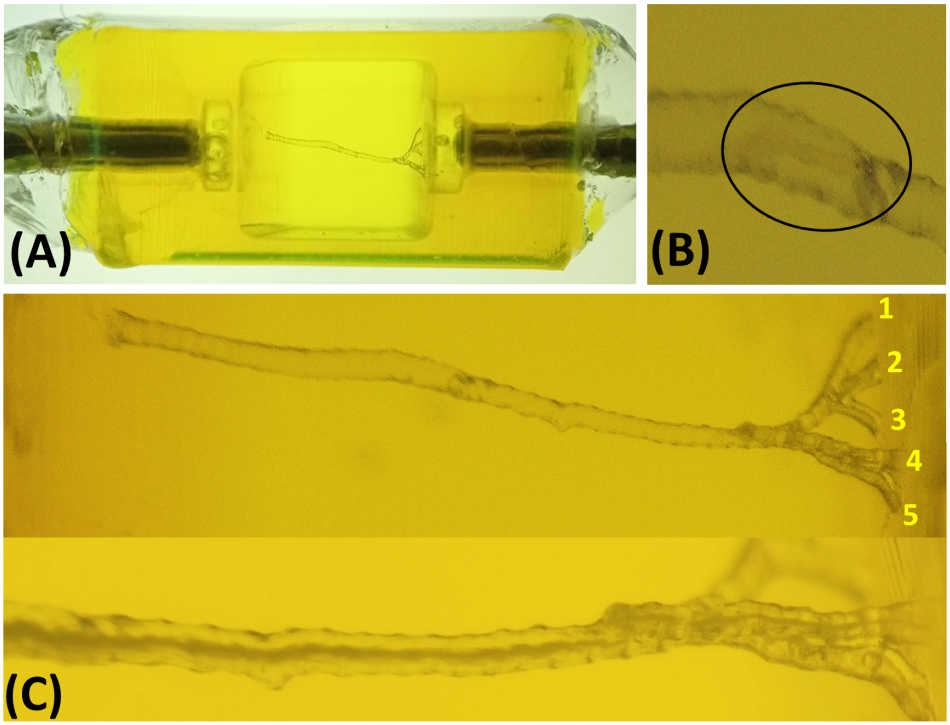

Figure 8.2: Model 1. (A) Optical microscope images after vat printing. (B) Blocked vessel. (C) Branches enumeration and flow mainly observable only in path 4.

The first consideration to do is that the curved shape of the main channel seems to be less prominent than the one in the stl file. The reason for this difference is probably related to the use of isopropanol to clean the structure from the uncured resin that has an effect on the cured resin as well if applied for long times, especially with such a thin wall thickness. Then, for next printings, the duration of the cleaning phase with isopropanol was minimized. The channel was then perfused with distilled water to clean it from isopropanol.

Since these first experiments, channel obstruction due to dust or agglomerates frequently occurred (Fig. 8.2B). It depended mainly on the micro dimensions and probably also on the shape of the inner lumen that wasn't smooth enough. Also, not enough attention was paid to avoid that external bodies could flow inside the microfluidic path. Thus, for further tests with other phantoms, it was given more earnest heed to not contaminate the fluid, for example cleaning the needle from abrasion residue and changing more frequently the syringes and tubes.
Changing the flow direction and using soapy water helped during these first evaluations, but the use of soap led to the formation of air bubbles into the fluid, as well as into the channel and inside the fluid collection chambers creating a non ideal condition. However, the air bubbles made the water opaque and was then possible to check the flow into the five paths. With reference to the numbers in Fig. 8.2C, path 1 was the only one in which any flow couldn't be observed. The other paths were open but, as expected frorm Fig. 8.1, path 4 is the one with the lower resistance and most of the flow was observed in that path. Obviously, this isn't an ideal condition because, if in some branches there is no flow, then they shouldn't be visible in the OCT angiography. After few tests, the hollow inner path was permanently obstructed and neither a sonicator bath managed to free the channel.

OCTA results

For this phantom, the OCT acquisitions were performed without the PDMS layers casting because of PDMS unavailability before the vessel was permanently blocked and became unusable. Then, the only available results are referred to a situation in which the vessel is surrounded by air. Whole milk was used as blood-mimicking fluid and water as reference. An intensity-based algorithm was implemented.

In Fig. 8.3 is shown the OCTA en-face extraction from the four OCT volumes setting a flow of 100 μl/min. As expected, the reflection artifact is quite strong and the depth range for the en-face extraction has been carefully chosen. Apparently, it seems that the OCTA properly highlights the path covered by the milk and with a threshold is possible to discriminate the signal from the steady vat and the signal from the flowing milk. Actually, comparing the result with the OCTA extracted for a 0 μl/min flow rate, the signal intensities are similar. Two points were fixed along the channel, one on the main channel and one on the branching point. Then, two sliding boxes located at a depth aligned with the points of interest were used to check for any differences between the steady and flowing milk at 5, 10 and 100 μl/min. The relative graphs are shown in Fig. 8.4. The only differences are due to a different noise level that affect the images, as it can be notice from the "baseline", i.e. the signal from pixel belonging to air.

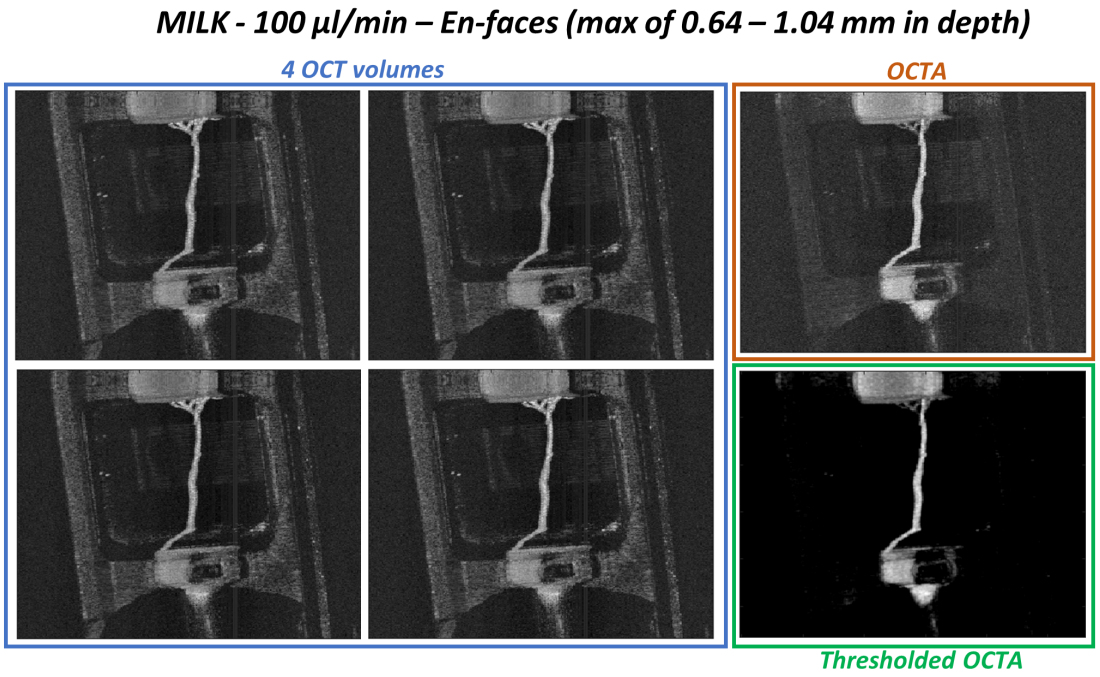

Figure 8.3: Model 1. From 4 OCT volume to iOCTA.

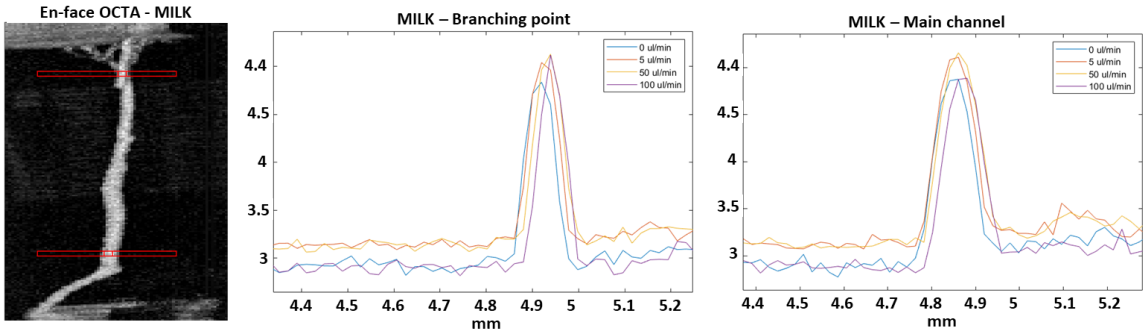

Figure 8.4: iOCTA signal from pixels inside a sliding box centered on the vessels. The upper box is called "branching point" and the lower one "main channel".

As mentioned before, unfortunately, the irreversible channel obstruction occurred before that any other experiments and evaluations could be done. However, this first printing was extremely useful.
First of all, from a printing point of view, the printability of realistic shapes below 100 μm in diameter was successfully verified and the difficulties faced to handle it allowed to understand the needs for next printings, that are mainly smoother surfaces and, at least for initial testings, avoiding inner diameters below 20 μm because of the risk to block the paths after few tests.
About the OCTA signal, the impossibility to discriminate fluid in static and dynamic

situations came to light. However, because of the absence of PDMS, the air-resin interface is not an ideal condition since the difference in refractive indexes leads to a strong reflection and projection artifacts that could totally cover the signal from the milk. Also, the axial resolution of the printer, i.e. the thickness of the printed layers, is 8 μm, comparable to the 1300 nm wavelength of the laser beam employed in the OCT system. Then, the possibility to have an OCTA signal due to the roughness of the resin surface must be taken into account.

Further tests with the vat filled by skin-mimicking layers must be performed.

8.1.2 Model 2 - Three branches model

This model was designed based on the needs arose testing the previous phantom, mainly the bigger inner diameters and a smoother internal surface to minimize the chances to block the vessels.

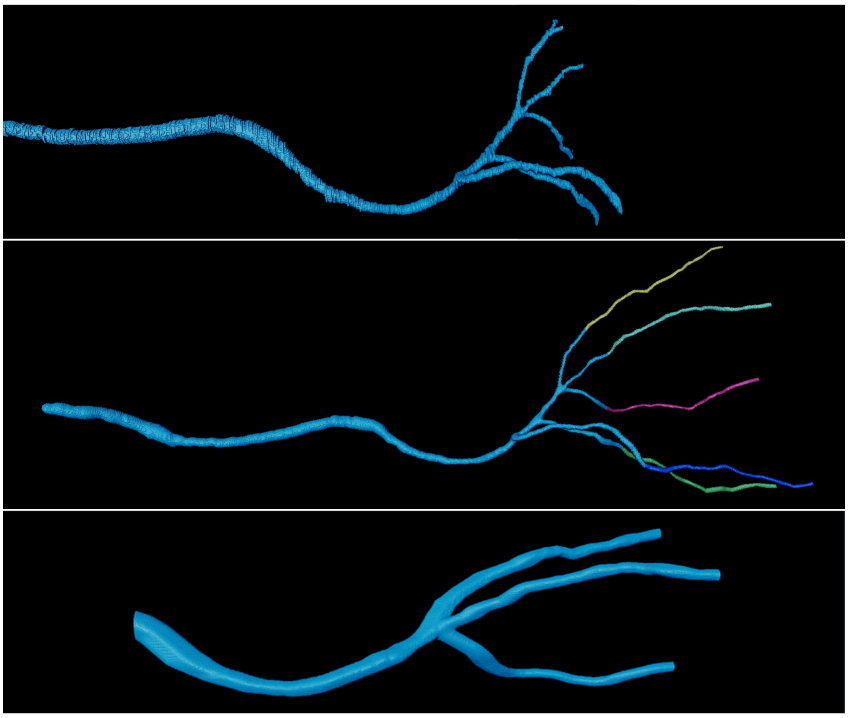

Figure 8.5: 3D modelling steps from model 1 to model 2.

The modeling phase was carried out starting from the previous model. As summarized in Fig. 8.5, the branches were elongated in order to have the branching point approximately in center of the field of view. Also, the vessel was simply dilated so that the minimum inner diameter could be higher than 100 µm and 3D smoothing was applied. Because of the bigger dimensions, 2 branches were discarded and the volume was cropped in length. The new branches were modeled exploiting the 3D space inside

the vat. Thus, they were used to investigate signal from different depths. In Fig. 8.6 are shown the details relative to the inner diameters and the branches depth, as well the comparison between the stl model and the printing result.

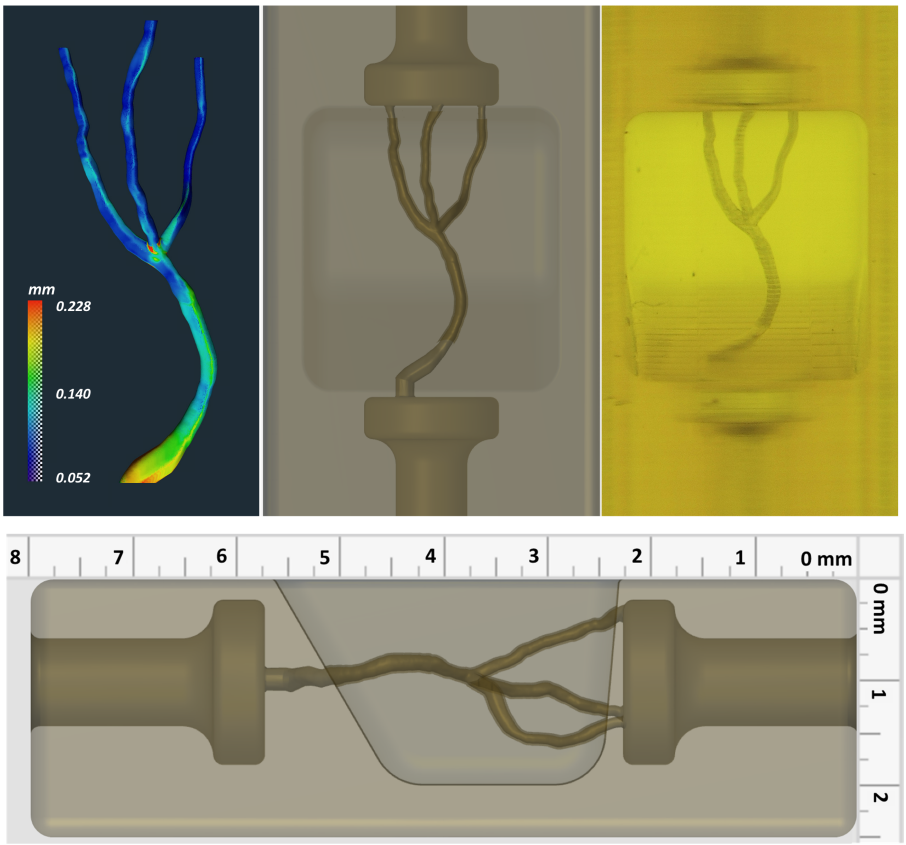

Figure 8.6: Model 2 details and optical microscope image of the printed model.

OCTA results

The phantom was firstly imaged with only the dermis layer. The OCT and iOCTA images are shown in Fig. 8.7 A. It can be seen that even if the epidermis layer is still missing, the signal from the deepest branch is lost, especially next to the vat edge where the PDMS thickness is higher and the vessel deeper. Also, as previously stated, the resin vat yields a signal that, when too many images are averaged for better visualization, became comparable to the one from the vessel. Then in Fig. 8.7 B are shown the segmented volume and the original one, obtaining an overlapping characterized by a Dice coefficient of 64%, mostly because of the deeper vessel that is not detected.
Then, the OCT imaging was performed again after adding the epidermis mimicking layer. The results are shown in Fig. 8.8. Because of the surface tension of PDMS in contact with the vat, the upper dermis layer surface results to have a concave shape and the epidermis layer shape will be complementary, obtaining an epidermis thickness not constant. However, the vasculature designs developed in this work are mostly located

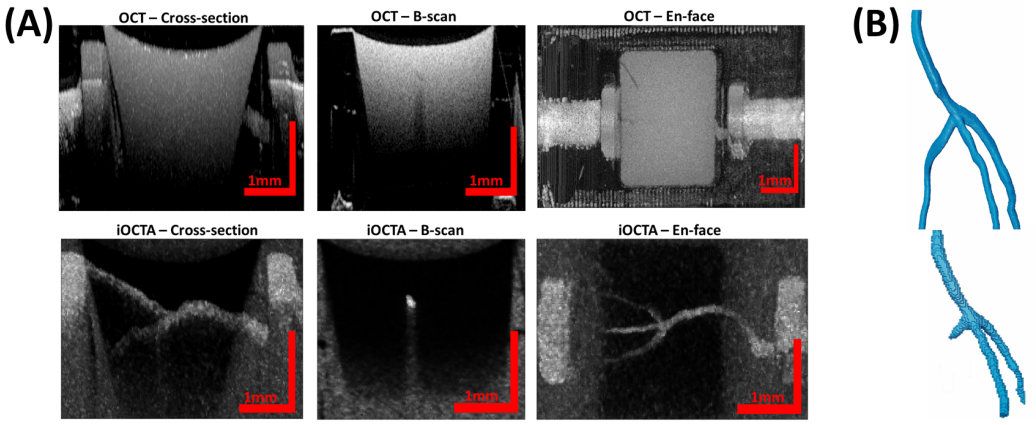

Figure 8.7: (A) OCT and iOCTA images of "model 2" phantom without the epidermis layer. (B) Original vessel model and OCTA segmentation, respectively.

in the central part of the vat. Then, the maximum epidermis layer is usually exploited and the thickness variability is negligible. Considering several B-scans, the epidermis thickness in the phantom is between 300 and 400 μm in the middle part, that results to be too thick with the effect that the signal in depth is lost and only the most shallow vessel is clearly distinguishable. To overcome this issue, one tested solution was to completely fill the vat with the dermis layer obtaining a flat surface and then overlap a thin layer of epidermis always obtaining a flat surface. This technique requires that vasculature is not designed too much in depth.
Thus, the layering of epidermis should be optimized.

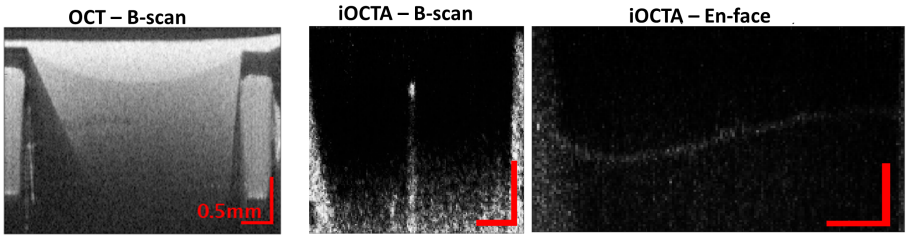

Figure 8.8: OCT and iOCTA images of "model 2" phantom with both the layers.

This phantom, with only the dermis, was also deeply exploited to characterize the OCTA signal - flow velocity relationship and the results are shown and discussed in section 7.3.

8.2 Pathological models

Both the phantoms described in this chapter come from the segmentation of an OCTA acquisition performed on a subject affected by CVI (Fig. 5.1(b)). Since the whole structure is quite complex to reproduce, some vessels were isolated and processed trying to preserve the peculiar shapes of a CVI pattern.

8.2.1 Model 3 - Bulky vessel

The first pathological model was extracted identifying the most significant pattern, mainly the dilated, tortuous and irregular shapes of the vessels. The processed version of the selected vessel is shown in Fig. 8.9.

In Fig. 8.9 is also reported the inner diameter map for this model, showing that the average diameter is around 500 μm, as in the original volume. The vessel wall was kept to 20 μm and not any critical issue emerged during printing. In the middle part of the model there is a bifurcation. One of the two branches has an inner diameter that is approximately the double of the other one but, since the minimum diameter is above 200 μm, the perfusion of all the paths shouldn't be an issue. Indeed, the cleaning phase with isopropanol didn't show any difficulty.
In the first image of Fig. 8.10, it can be seen, through the optical microscope, the check with blue ink for any printing imperfections and both the branches result to be properly open.

However, some problem occurred during PDMS casting. In particular, during the curing phase in the oven, the PDMS in the vat overflowed and the PDMS distribution became irregularly with some air between the dermis layer and the vat floor. Since the steps were the same followed for previous assembling, the reason for this behavior could be related to the bigger and irregularly shape of the vessel, so that when the PDMS touched it before depositing inside the vat, some air was embedded. Thus, more attempts were needed to have a properly assembled phantom and the curing phase was made at room temperature to avoid any other difficulty. Even if more attention was paid and the air bubble inclusion was solved, further issues with PDMS was observed since it seems that during the PDMS curing phase, especially with such a irregular and bigger shape, the PDMS tends to trace the morphology of the underlying sructure, independently from the PDMS surface shape before curing.

OCTA results

The OCT and iOCTA images are shown in Fig. 8.10. From the OCT B-scan, the shape of the epidermis layer can be assessed and the maximum thickness was quantified to be about 400 μm. The iOCTA shown a proper reconstruction, even if the projection artifact has an important impact on the quality of the images that made the segmentation too challenging. Again, the epidermis layering and composition result to be critical and must be optimized.

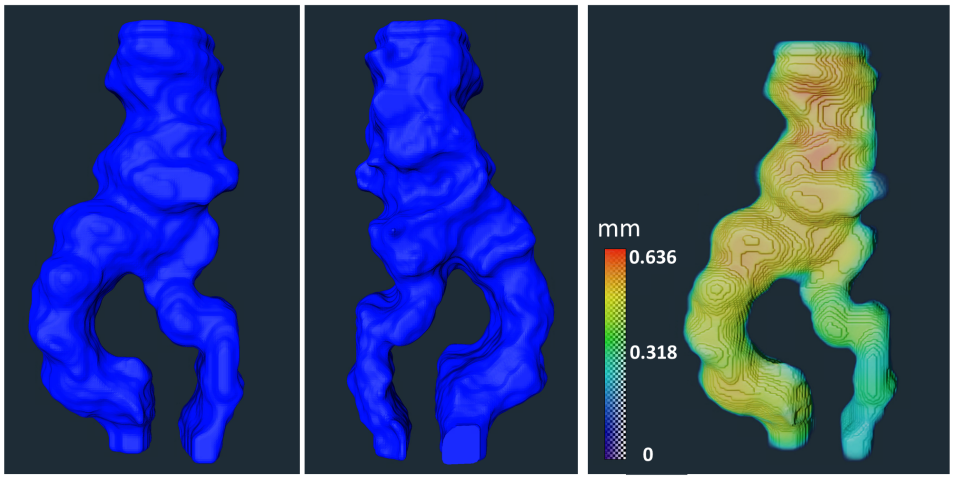

Figure 8.9: 3D model of the internal lumen of "Model 3" an relative diameter map.

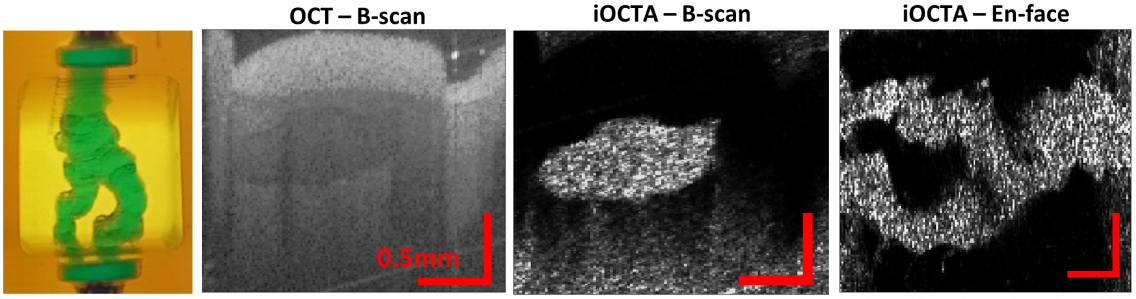

Figure 8.10: Model 3: image through optical microscope perfusing the phanatom with blue ink before PDMS pouring and the OCT and iOCTA images extracted after phantom assembly.

8.2.2 Model 4 - two ins two outs

Similarly to the previous model, a second vessel was extracted from the pathological OCTA volume and further processed. This morphology was chosen because of the interest into testing higher levels of morphological complexity both from the printing and OCTA algorithm point of view.

The model is shown in Fig. 8.11. It's characterized by two inlets and two outlets and the main channel has a "U" shape in the middle part. From the inner diameter map in the same figure, the average diameter is around 400 μm and also in case, in the lower part of the image, one of the two branches should have a resistance that is approximately half of the other one. However, also in this case the ink perfusion didn't highlight any critical issue and the vessel wall was kept to 20 μm.
In the first image of Fig. 8.12, it can be seen, through the optical microscope, the check with blue ink for any printing imperfections and all the branches result to be properly open.

Also, the curing phase turned out to be critical for this phantom as well and the same considerations made for the previous phantom shall also be applied in this case. Then, a slightly different approach for PDMS was testes. Even if the vasculature was located quite in deep, the dermis layer was poured to fill the entire vat. Then, a drop of epidermis was poured on the surface and leveled as thin as possible.

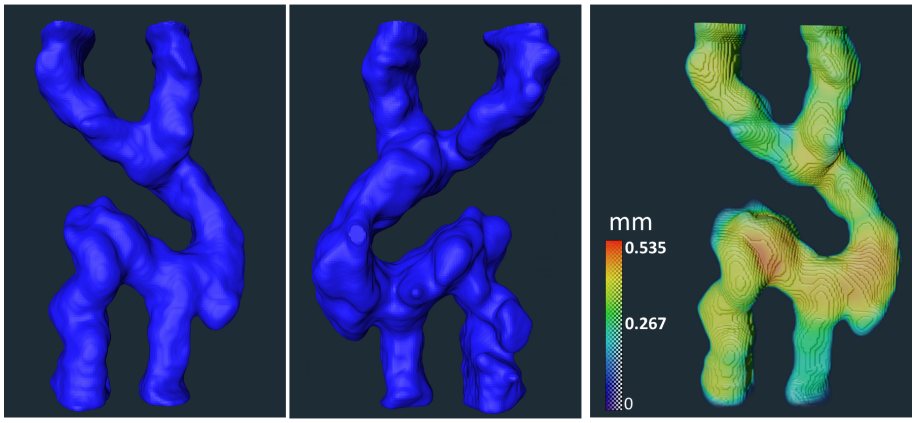

Figure 8.11: 3D model of the internal lumen of "Model 4" an relative diameter map.

OCTA results

In Fig. 8.12 are collected the OCT and iOCTA images extracted from this phantom. Better results in terms of epidermis thickness were observed. Indeed, the OCT B-scan shows that the epidemris layer should about 100 μm in thickness and also the upper surface is more regular. Even if the depth of the vessel location still affects the OCTA images quality, the segmentation could be extracted, resulting into a overlapping respect to the original model of 70% in terms of Dice coefficient.

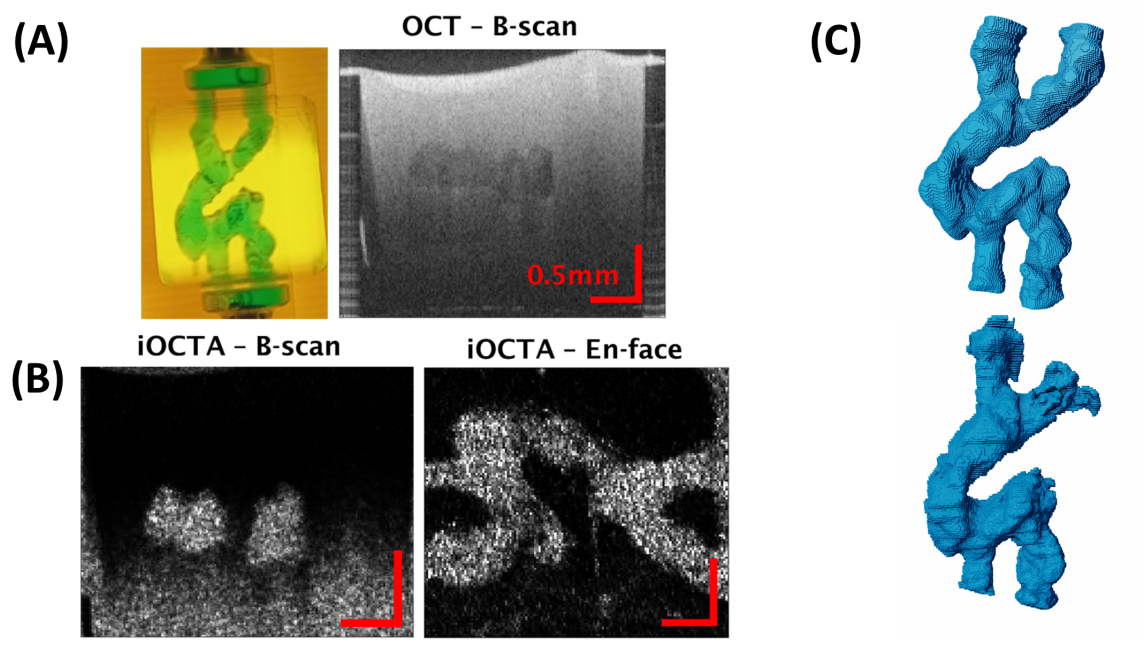

Figure 8.12: Model 4: (A) image through optical microscope perfusing the phanatom with blue ink before PDMS pouring; (B) OCT and iOCTA images extracted after phantom assembly; (C) the original vessel model and the OCTA segmentation, respectively.

9. Capillary-mimicking phantom

The previous results have shown how the proposed approach is capable to accurately mimic both healthy and pathological vasculature morphology as well as their perfusion. However, since the inner diameters of the four reported models are above 20 μm, they can mainly be considered as arterioles or venules. The results collected in this chapter investigate, instead, the possibility to successfully print channels with inner diameters down to 20 μm and then realistic capillary network characterized by even thinner lumens.

9.1 Preliminary printings

In Fig. are shown the first printing attempts of straight channels with internal diameters of 40 μm and 20 μm. Each printing contains five parallel replica of the same channel so that more than one attempt could be evaluated exploiting only one printing session. In these cases, the wall thickness was reduced to 16 μm for both diameters. Red ink was used to check for lumen integrity.

In both cases (Fig. 9.1A and 9.1C), it's possible to see that isopropanol channel perfusion affects the straight shape of the channels that now don't appear exactly parallel as just after printing. Considering the reduced vessel wall thickness, it was expected.
Regarding the 40 μm channels, the perfusion with red ink revealed that all the five channels were open (Fig. 9.1B).
About the 20 μm channels, since the first test, for one out of five paths a leakage could be observed again at the same position of the leakage of the 40 μm diameter printing (Fig. 9.1C). In order to check at least for the integrity of the lumen as well as for the others four channels, a small amount of glue was dropped on the point of leakage, covering obviously all the five paths that were then perfused (Fig. 9.1E). The weight of the glue drop caused the channel interested by the leakage to be drastically deformed. Anyway, it's possible to observe that all the five lumen are properly open.
Thus, such structures are printable but attention must be paid to the inlet and outlet vessel shape.

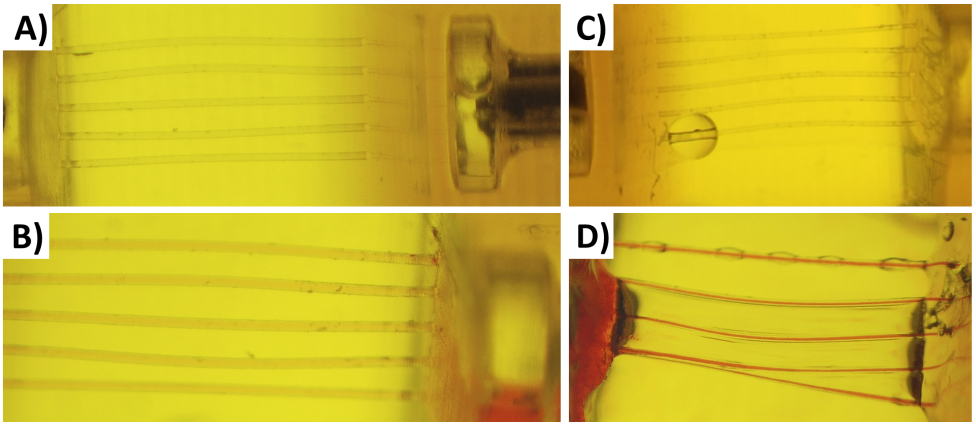

Figure 9.1: (A) and (B) show the printed 40 μm straight channels and their perfusion with diluted red ink. (C) show the printed 20 μm straight channels with a leakage. Fixing the leakage with glue, the flowing red ink is shown in (D).

9.2 Capillary network phantom

Once verified that such small lumens are printable, the aim was to further verify the printability of realistic morphologies characterized by inner diameters around 20 μm or even thinner. Thus, a portion with the smallest vessels was taken from the pathological angiography. The structure was cleaned from incomplete bifurcations and two inlets were identified. Then, this structure was merged with its mirrored version so that a complex capillary network with two inlets and two outlets could be obtained. Finally, the model was smoothed and scaled to the desired dimensions. These steps are summarized in Fig. 9.2.

As shown in Fig. 9.2, the inner diameters of the capillary network are mainly between 20 and 10 μm, with the minimum diameter of about 8 μm.
Because of the leakage problems with the preliminary printings, the inlet and outlet paths were dilated in the point were they're merged with the vat. Also, since the overall dimensions of the capillary network are smaller, the vat length was modified to match the network length, around 1 mm, and then also the empty space in the vat for PDMS pouring was significantly reduced, making PDMS casting more critical. Finally, the four repetitions of the same capillary network lumen were merged with the vat. Since the network lies mostly on the same plane, two models were oriented horizontally and the other two were oriented with a 45° tilt angle respect to the vat upper surface. The couples of model characterized by the same inclination were located at different depth, about 300 μm and 700 μm from the upper surface. The 3D model is shown in Fig. 9.3 A.

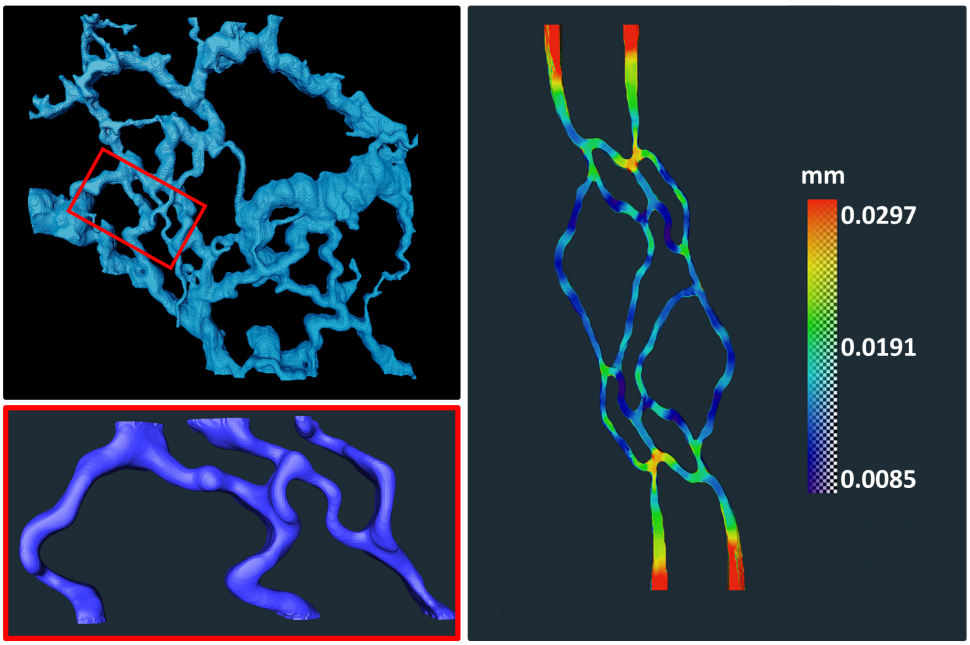

Figure 9.2: Capillary network design. The volume inside the red box was extracted and processes obtaining the final model with a diameter map shown on the right.

9.2.1 Printing results

Two printings were done with a 10x objective lens trying both a *simple* and a *voxel* printing modality, shown in Fig. 9.3 B and Fig. 9.3 C, respectively. In both cases, the isopropanol flowing phase wasn't so easy as in the previous cases. In a first moment it wasn't clear if it was due to the failure of printing such thin hollow vessels or to the difficulty in dissolving uncured resin in diameters below 20 μm. Indeed, if the contact area between uncured resin and isopropanol is so small and also the resin cannot be moved because of the very high resistance of the 10 μm vessels, then putting in contact new isopropanol with the not dissolved resin is challenging. In Fig. is possible to see that the initial parts of each network are open. Some techniques able to put in motion the isopropanol inside the phantom should be applied, such as a sonicator bath. However, the risk is to irremediably destroy the thin structures. Then, before this kind of tests, further printings with a 20x objective lens were done in order to be sure that the main issue is not related to the printing itself. Even if a first attempt was characterized by some holes in the polymerized resin of the vat because of a wrong setting of the laser power, the capillary network wasn't interested by these errors. Thus, the isopropanol flowing phase was performed using the infusion pump and not any difficulty was found. As it can be seen in Fig. 9.3 D, all the paths of the foure networks are properly open and the whole morphology doesn't seem to be compromised by isopropanol.
Thus, the previous failures were probably due to the printing itself. Indeed, even if the 10x objective leads to a transversal resolution of 0.5 μm, the axial resolution is 5 μm. The minimum diameter is 8 μm considering transversal slicing but the structures are highly complex along the axial direction. Thus, the printing failure with the 10x

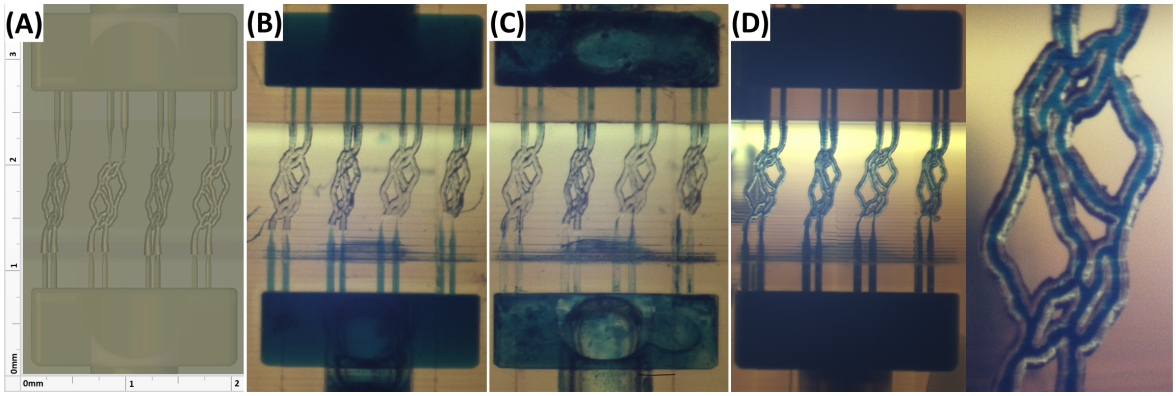

Figure 9.3: (A) STL file. (B) Phantom printed with the 10x objective lens and the simple mode. (C) Phantom printed with the 10x objective lens and the voxel mode. (D) Phantom printed with the 20x objective lens and the voxel mode with a zoom on one network.

objective lens is reasonable.
Then, another printing with 20x objective lens was repeated to fix the issues related to the laser power settings.

9.2.2 PDMS pouring

As mentioned before, the dimensions of the vat were reduced in order to accommodate the capillary networks. A consequence is that the pouring of PDMS is more critical since the space is not enough to easily drop it directly on the vat floor. If PDMS passes through the network during pouring, the risk is to include air again inside the layer. Then, a 0.5 mm needle was used to pour PDMS directly on the internal floor of the vat.

9.2.3 OCTA results

Since both the axial and lateral resolution of the OCT system are bigger than the diameters of the printed capillary networks, it wasn't expected to reconstruct the modelled geometry starting from the angiography. However, a weak OCTA signal was observed since content of the voxels containing the lumens changes. In Fig. 9.4 is shown an OCT B-scan and an OCTA en-face. Using the diluted whole milk as in the previous experiments could be critical since the particles inside the milk have dimensions comparable to the networks diameters. Indeed, from the OCTA image seems that not all the four networks are open. Also, since the OCTA en-face is obtained performing the median along 5 pixels in depth to attenuate the noise, the only network that gives a signal is the one tilted with an angle of 45 degree respect to the surface because some branches are overlapped from the en-face point of view. The other tilted network is not visible probably because blocked. More suitable blood mimicking fluids should be used.

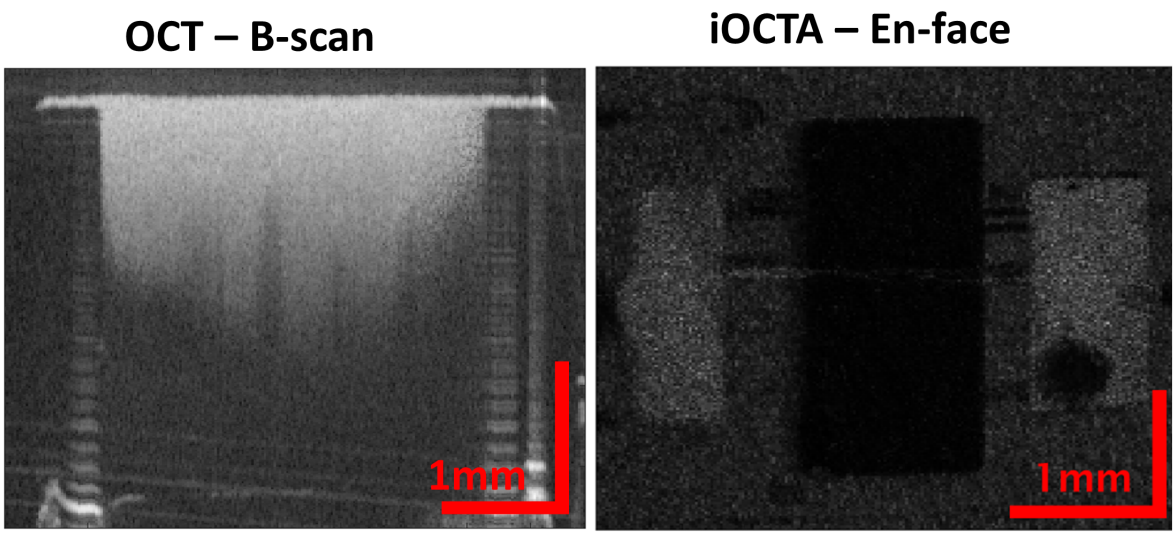

Figure 9.4: Capillary networks phantom: (A) OCT B-scan; (B) iOCTA en-face.

However, the printability of such phantoms makes this development approach a potential recipe for micro-OCT phantoms.

Part IV

Conclusions

In this thesis, a quite innovative approach for optical skin mimicking phantom development was presented. Several tests were performed in order to prove that the proposed approach is capable of mimicking the skin from different points of view:

- The multi-layered architecture is achievable because of the selected bulk material, PDMS, that takes the shape of a specially designed vat and, after curing, is stable over time, even for years if properly stored. Then, two layers of PDMS can be stratified.

- Simply adding black and white silicone pigments to the PDMS before curing is possible to match the optical properties of skin layers. The additives concentrations depend on the laser source wavelength. At 1300 nm, in order to mimic the absorption and reduced scattering coefficient values from literature, the optimal values for black and white pigments were set to be 0.18% and 0.36% for dermis and 0.20% and 0.72% for epidermis, respectively. The resulting optical properties in terms of reduced scattering coefficient and absorption coefficient are 1.07 $mm^{-}1$ and 0.32 $mm^{-}1$ for dermis and 1.98 $mm^{-}1$ and 0.48 $mm^{-}1$ for epidermis, respectively. However, further tests are needed to optimize the skin mimicking layers composition from an OCT point of view and others coefficients must be taken into account.

- Realistic microvasculature mimicking morphologies can be embedded into the PDMS layers thanks to the 2PP 3D-printing technique that, depending on the printer set up, can achieve printing resolution down to hundreds of nanometers. Then, increasing levels of complexity were proven to be printable mimicking both healthy and pathological morphologies as well as capillary networks.

- The most important feature of such printed structures relies on the possibility to perfuse them. The desired vasculature design is used as model for the hollow lumen on which a certain wall thickness can be added. The wall thickness value of 20 μm resulted to be thick enough to preserve structure integrity without appreciably affecting the OCTA segmentations. Inner diameters down to 8 μm were printed.

However, some limitations emerged during phantoms development and further tests should be performed to overcome them:

- The main issue of this approach as it was described is that the layers thickness and the interface shape are not accurately tunable. It was observed that the PDMS-additive mixture changes its shape after curing. Indeed, even if the surface of the layer is flattened after pouring, independently from the curing temperature, the PDMS layers seem to retrace the vasculature shapes, especially with bigger and more irregular vessels such as the pathological ones. Then, there isn't a direct control on the thickness, especially for epidermis, with the risk to have a too thick layer that, considering the penetration depth of the OCT system of 1.5 mm, could hide all the information. Also, since the layers will be complementary, the interface shape will be affected by this aspect.

To overcome this issue, a solution could be modifying the vat design so that the vasculature can be closer to the upper surface of the phantom. Then, the vat can be completely filled by the dermis mixture paying attention to observe the superficial tension effect of the phantom with the upper extermity of the phantom. In this way, hopefully, the superficial tension should avoid that the PDMS could retrace the shape of the underlying vasculature. Then, a thin epidermis layer can be applied dropping the epidermis mixture of the phantom surface and remove it flattening it. Thus, a very thin layer of PDMS will cure on phantoms. Preliminary attempts seem to show better results, for instance obtaining a 70% overlapping percentage for a pahtological model, but further tests are needed.

- PDMS pouring phase is critical also because of the risk to incorporate air bubble inside the layers if the PDMS goes through the vasculature and drips on the vat floor. Thin needles must then be used to directly pouring the PDMS on the vat floor but, considering the dimension of the vat printed during his work, a damage of the micrometric vessels can occurs. Then, the vat design should be rearranged in a way that more PDMS could surround the vessels, both below and on the sides.

- Also, it must be taken into account that, when the structures are particularly thin and elongated, the use of isopropanol to clean the structure from uncured resin is critical. As shown with the first phantom (Fig. 8.2), the isopropanol can potentially affect the initial shape. With vessels characterized by more branches, this issue wasn't observed.

It was shown the potential of developed phantoms to test the OCT system skills, with the possibility to compare the segmentation result with the exact model that was imaged and quantify system accuracy and signal loss in depth. Also, it could be a useful tool for OCTA algorithms characterization.

Furthermore, a characterization of the OCTA signal respect to interscan time and flow velocity was performed and the possibility to use a realistic phantom had the role to highlight the differences between a more simple but unrealistic test and an in vivo mimicking experimental set-up.

In conclusion, this approach can potentially become a reference for realistic optical skin phantom development, especially for research purpose. Extending the PDMS mixtures characterization to other properties, these phantoms could be used in multimodal imaging application as well, such as OCT-PAI systems.

Bibliography

[1] A. F. Fercher, W. Drexler, C. K. Hitzenberger, and T. Lasser, "Optical coherence tomography - principles and applications," *Reports on Progress in Physics*, vol. 66, p. 239, jan 2003.

[2] W. Drexler, M. Liu, A. Kumar, T. Kamali, A. Unterhuber, and R. A. Leitgeb, "Optical coherence tomography today: speed, contrast, and multimodality," *Journal of Biomedical Optics*, vol. 19, no. 7, p. 071412, 2014.

[3] K. M. Meiburger, Z. Chen, C. Sinz, E. Hoover, M. Minneman, J. Ensher, H. Kittler, R. A. Leitgeb, W. Drexler, and M. Liu, "Automatic skin lesion area determination of basal cell carcinoma using optical coherence tomography angiography and a skeletonization approach: Preliminary results," *J Biophotonics*, vol. 12(9):e201900131, 2019.

[4] J. Zhu, C. W. Merkle, M. T. Bernucci, S. P. Chong, and V. J. Srinivasan, "Can oct angiography be made a quantitative blood measurement tool?," *Applied Sciences*, vol. 7, no. 7, 2017.

[5] Z. Chen, M. Liu, M. Minneman, L. Ginner, E. Hoover, H. Sattmann, M. Bonesi, W. Drexler, and R. A. Leitgeb, "Phase-stable swept source oct angiography in human skin using an akinetic source," *Biomed. Opt. Express*, vol. 7, pp. 3032–3048, Aug 2016.

[6] A. Zhang, Q. Zhang, C.-L. Chen, and R. K. Wang, "Methods and algorithms for optical coherence tomography-based angiography: a review and comparison," *Journal of Biomedical Optics*, vol. 20, no. 10, p. 100901, 2015.

[7] R. F. Spaide, J. G. Fujimoto, N. K. Waheed, S. R. Sadda, and G. Staurenghi, "Optical coherence tomography angiography," *Progress in Retinal and Eye Research*, vol. 64, pp. 1–55, 2018.

[8] W. J. Choi, W. Qin, C.-L. Chen, J. Wang, Q. Zhang, X. Yang, B. Z. Gao, and R. K. Wang, "Characterizing relationship between optical microangiography signals and capillary flow using microfluidic channels," *Biomed. Opt. Express*, vol. 7, pp. 2709–2728, Jul 2016.

[9] M. Stücker, V. Baier, T. Reuther, K. Hoffmann, K. Kellam, and P. Altmeyer, "Capillary blood cell velocity in human skin capillaries located perpendicularly to

the skin surface: Measured by a new laser doppler anemometer," *Microvascular Research*, vol. 52, no. 2, pp. 188–192, 1996.

[10] D. Richter, A. M. Fard, J. Straub, W. Wei, Q. Zhang, and R. K. Wang, "Relative retinal flow velocity detection using optical coherence tomography angiography imaging," *Biomed. Opt. Express*, vol. 11, pp. 6710–6720, Nov 2020.

[11] M. Liu and W. Drexler, "Optical coherence tomography angiography and photoacoustic imaging in dermatology," *Photochem. Photobiol. Sci.*, vol. 18, pp. 945–962, 2019.

[12] T. Cammarota, F. Pinto, A. Magliaro, and A. Sarno, "Current uses of diagnostic high-frequency us in dermatology," *European Journal of Radiology*, vol. 27, pp. S215–S223, 1998.

[13] A. J. Deegan and R. K. Wang, "Microvascular imaging of the skin," *Physics in Medicine & Biology*, vol. 64, p. 07TR01, mar 2019.

[14] S. Standring, *Gray's anatomy e-book: the anatomical basis of clinical practice*. Elsevier Health Sciences, 2021.

[15] I. Bentov and M. J. Reed, "The effect of aging on the cutaneous microvasculature," *Microvascular Research*, vol. 100, pp. 25–31, 2015.

[16] A. Bollinger, P. Butti, J. P. Barra, and W. Siegenthaler, "Red blood cell velocity in nailfold capillaries of man measured by a television microscopy technique," *Microvascular Research*, vol. 7, no. 1, pp. 61–72, 1974.

[17] R. T. Eberhardt and J. D. Raffetto, "Chronic venous insufficiency," *Circulation*, vol. 130, no. 4, pp. 333–346, 2014.

[18] E. V. Salomatina, B. Jiang, J. Novak, and A. N. Yaroslavsky, "Optical properties of normal and cancerous human skin in the visible and near-infrared spectral range," *Journal of Biomedical Optics*, vol. 11, no. 6, p. 064026, 2006.

[19] B. W. Pogue and M. S. Patterson, "Review of tissue simulating phantoms for optical spectroscopy, imaging and dosimetry," *Journal of Biomedical Optics*, vol. 11, no. 4, p. 041102, 2006.

[20] L. Hacker, H. Wabnitz, A. Pifferi, T. Pfefer, B. Pogue, and S. Bohndiek, "Criteria for the design of tissue-mimicking phantoms for the standardization of biophotonic instrumentation," *Nature Biomedical Engineering*, vol. 6, pp. 541–558, 05 2022.

[21] A. Bhatti, T. Ishii, and Y. Saijo, "A micro-flow phantom for superficial microvasculature imaging," *Journal of Physics: Conference Series*, vol. 2071, p. 012054, 10 2021.

[22] G. Lamouche, B. F. Kennedy, K. M. Kennedy, C.-E. Bisaillon, A. Curatolo, G. Campbell, V. Pazos, and D. D. Sampson, "Review of tissue simulating phantoms with controllable optical, mechanical and structural properties for use in optical coherence tomography," *Biomed. Opt. Express*, vol. 3, pp. 1381–1398, Jun 2012.

[23] A. Bykov, A. Popov, A. Priezzhev, and R. Myllylä, "Multilayer tissue phantoms with embedded capillary system for oct and doct imaging," *Proc SPIE*, vol. 8091, 06 2011.

[24] C. Chen, M. Ahmed, T. Häfner, F. Klämpfl, F. Stelzle, and M. Schmidt, "Fabrication of a turbid optofluidic phantom device with tunable μa and μ's to simulate cutaneous vascular perfusion," *Scientific Reports*, vol. 6, p. 30567, 07 2016.

[25] A. Goldfain, P. Lemaillet, D. Allen, K. Briggman, and J. Hwang, "Polydimethylsiloxane tissue-mimicking phantoms with tunable optical properties," *Journal of Biomedical Optics*, vol. 27, 11 2021.

[26] J. Wang, J. Coburn, C.-P. Liang, N. Woolsey, J. C. Ramella-Roman, Y. Chen, and T. J. Pfefer, "Three-dimensional printing of tissue phantoms for biophotonic imaging," *Opt. Lett.*, vol. 39, pp. 3010–3013, May 2014.

[27] G. Liu, K. Huang, Q. Jia, S. Liu, S. Shen, J. Li, E. Dong, P. Lemaillet, D. W. Allen, and R. X. Xu, "Fabrication of a multilayer tissue-mimicking phantom with tunable optical properties to simulate vascular oxygenation and perfusion for optical imaging technology," *Appl. Opt.*, vol. 57, pp. 6772–6780, Aug 2018.

[28] C. Little, R. Poduval, R. Caulfield, S. Noimark, R. Colchester, C. Loder, M. K. Tiwari, R. Rakhit, I. Papakonstantinou, and A. Desjardins, "Micron resolution, high-fidelity three-dimensional vascular optical imaging phantoms," *Journal of biomedical optics*, vol. 24, pp. 1–4, 02 2019.

[29] J.-F. Xing, M.-L. Zheng, and X.-M. Duan, "Two-photon polymerization microfabrication of hydrogels: an advanced 3d printing technology for tissue engineering and drug delivery," *Chem. Soc. Rev.*, vol. 44, 05 2015.

[30] F. Franco Martinez, C. Grasl, E. Kornfellner, M. Vostatek, A. Cendrero, F. Moscato, and A. Diaz Lantada, "Hybrid design and prototyping of metamaterials and metasurfaces," *Virtual and Physical Prototyping*, vol. 2022, pp. 1–16, 07 2022.

[31] L. Veselka, L. Krainz, L. Mindrinos, W. Drexler, and P. Elbau, "A quantitative model for optical coherence tomography," *Sensors*, vol. 21, no. 20, 2021.

[32] Y. Jia, O. Tan, J. Tokayer, B. Potsaid, Y. Wang, J. J. Liu, M. F. Kraus, H. Subhash, J. G. Fujimoto, J. Hornegger, and D. Huang, "Split-spectrum amplitude-decorrelation angiography with optical coherence tomography," *Opt. Express*, vol. 20, pp. 4710–4725, Feb 2012.